Gravity analysis of Parga and Hecate chasmata: Implications for rift and corona formation

Suzanne E. Smrekar,[1] Trudi Hoogenboom,[2] Ellen R. Stofan,[3] and Paula Martin[4]

[1]   The two largest rift systems on Venus, Parga, and Hecate chasmata contain one third of all coronae. We map variations in elastic thickness and apparent depth of compensation (ADC) in these two regions using the admittance function for gravity and topography. We examine the relationship between rifting and coronae by comparing lithospheric structure with corona characteristics including volcanism, topographic shape, fracture pattern, diameter, and stratigraphic age. At Hecate chasmata, both ADC and elastic thickness correlate with two main rift branches, the fracture style and corona characteristics. Hecate chasma thus appears to be dominated by extensional processes. Parga chasma shows little correlation between lithospheric properties and the location of coronae or rift segments. The ADC at Hecate and Parga chasmata is mostly less than 75–100 km, implying that there is not large-scale upwelling underlying the rift systems. The variations in the corona population sizes between Parga chasma, which has 131 coronae, and Hecate chasma, with 50 coronae, suggest differences in the evolution of the two rift systems. The much larger population of coronae at Parga contains more small coronae, many of which have relatively low volcanism and post date the rift. Further, many of the small coronae occur in chains and have similar diameters, as predicted by Rayleigh-Taylor type instabilities. These characteristics suggest that the smaller coronae may form via a later, secondary decompression melting phase. Thus, Hecate chasma may be younger than Parga chasma and could experience a secondary stage of corona formation in the future.

1.   Introduction

[2]   Parga and Hecate chasmata are the longest rift systems on Venus, with lengths of 10,000 and 8000 km, respectively. They define two sides of the Beta-Atla-Themis triangle or the BAT zone (Figure 1). Beta, Atla, and Themis regions have been interpreted to be hot spots [*Basilevsky et al.*, 1986; *McGill*, 1994; *Stofan and Smrekar*, 2005], based on their broad topographic rises, thin elastic lithospheres, deep apparent depths of compensation, volcanic centers, and uplift-related rifts. Overall, the BAT zone has a high concentration of volcanic features and coronae [*Head et al.*, 1992]. This area has been proposed to be the site of a superplume, multiple mantle plumes, or broad linear upwellings beneath the rifts [*Crumpler et al.*, 1993, 1997]. The dearth of impact crater halos in the region and the overall low population of craters implie that the region is relatively young [*Phillips et al.*, 1992;

Phillips and Izenberg, 1995]. Others have proposed that extension in the rift zones has enhanced volcanism through decompression melting [*Herrick and Phillips*, 1992; *Hansen and Phillips*, 1993]. *Sandwell and Schubert* [1992a, 1992b] proposed an alternative explanation that the fracture zones were subduction zones rather than extensional zones. However, most geologic studies find that the tectonic features are more consistent with extensional zones [*Hansen* 2000; *Hamilton and Stofan*, 1996].

[3]   The origin of these extremely long fracture zones on a planet without plate tectonics is puzzling. There are no apparent zones of compression or subduction that accommodate extension. This suggests that the amount of extension is small. In most locations, extension is difficult to estimate directly. Venusian chasmata have some similarities with terrestrial continental extensional zones and mid-ocean ridges. Although Parga and Hecate have hot spots located at either end, they clearly extend beyond the topographic rises that can produce uplift and related rifting. They are much longer than terrestrial rift systems associated with hot spots. The largest such system on Earth is the East African rift system, which is approximately 3500 km long or less than half the length of Hecate or Parga chasmata. Although they are comparable in length to some of the mid-ocean ridge segments, their morphology is quite different. Each rift has

[1]Jet Propulsion Laboratory, California Institute of Technology, Pasadena, California, USA.
[2]ExxonMobil, Gravity-Magnetics Group, Houston, Texas, USA.
[3]Proxemy Research, Laytonsville, Maryland, USA.
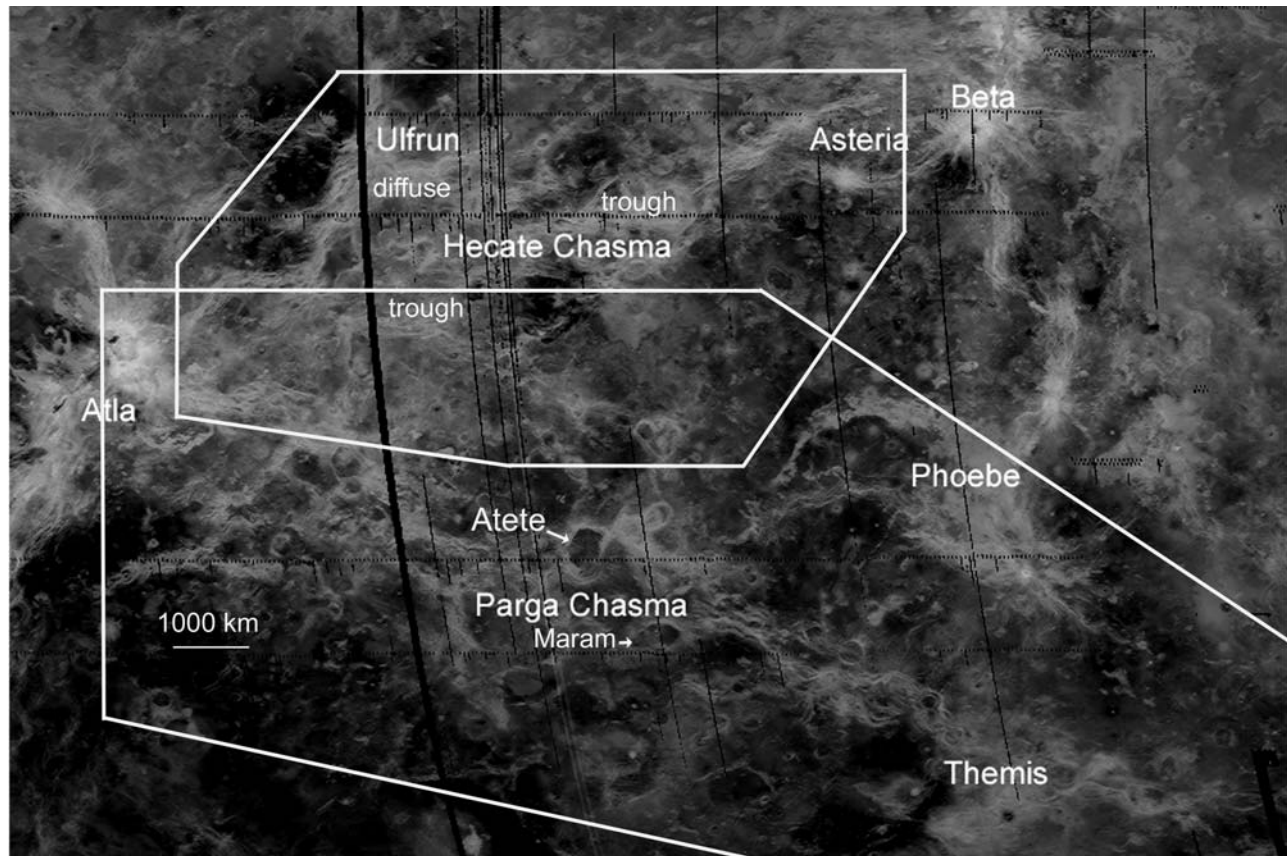[4]Department of Earth Sciences, Durham University, Science Laboratories, Durham, UK.

Figure 1. Left-looking Magellan radar image (50°S–35°N, 190°E–310°E) of Hecate and Parga chasmata. North is up. Brightness is primarily a function of roughness at the scale of the radar wavelength (~12 cm), with rougher regions, such as the chasmata, showing up as brighter. Radar facing slopes also appear brighter. White boxes indicate the locations of areas analyzed for Hecate and Parga chasmata.

multiple branches, extending at various angles relative to the main trend. Extension is generally distributed rather than localized along a single axis. There is no gravity high similar to that observed along mid-ocean ridges.

[4] One characteristic of Parga and Hecate chasmata is the strong concentration of coronae, features that are unique to Venus. Coronae are volcano-tectonic features, generally circular in shape with diameters ranging from 60 to 1060 km, with an average of 250 km [*Glaze et al.*, 2003]. A wide range of formation models have been proposed for coronae, including small-scale mantle upwelling [*Basilevsky et al.*, 1986; *Stofan et al.*, 1991; *Janes et al.*, 1992; *Koch and Manga*, 1996], delamination [*Hoogenboom and Houseman*, 2006], a combination of both [*Smrekar and Stofan*, 1997], subduction [*Sandwell and Schubert*, 1992a, 1992b], melt generation [*Tackley and Stevenson*, 1991, 1993; *Dombard et al.*, 2007], and compositional diapirs [*Hansen*, 2003]. Approximately one quarter (131 out of ~513) of all coronae on Venus occur in association with Parga chasma. The relationship between coronae and rift zones remains controversial [*McGill*, 1994; *Hamilton and Stofan*, 1996; *Herrick*, 1999; *Bleamaster and Hansen*, 2004; *Martin et al.*, 2007]. Do rifts from in regions where coronae have thinned the lithosphere via mantle upwelling? Or can coronae form more easily on lithosphere thinned by extension? Or some combination? Although most plains rifts have coronae, and the majority

(62%) of coronae occur along rifts or fracture belts [*Stofan et al.*, 1997; *Stofan et al.*, 2001], rifts and coronae also occur in isolation. Coronae also occur beyond the zone of extension, as defined by the troughs and fractures. There is stratigraphic evidence that coronae form before, after, or, most commonly, during rift formation [*Baer et al.*, 1994; *McGill*, 1994; *Hamilton and Stofan*, 1996; *Martin et al.*, 2007].

[5] *Martin et al.* [2007] studied rifting and coronae in Parga chasma, examining the characteristics of the rifts (rift width and depth, fracture width, depth and intensity) and the coronae (e.g., amount of volcanism, stratigraphic age with respect to the rift, etc.). Contrary to expectations from a visual inspection, statistical analysis shows that coronae at Parga chasma are randomly distributed with respect to the location of the nearest rift [*Martin et al.*, 2007]. The synchronous formation of coronae and rifting does, however, indicate that they are genetically related. They also investigated the possibility that coronae themselves load the lithosphere, creating tensile stress via magmatic hydrofracture at local tensile maxima of flexural and membrane stresses, as proposed for terrestrial oceanic volcanic chains [*Hieronymous and Bercovici*, 2000]. *Martin et al.* [2007] rejected this hypothesis for two reasons. First, fracture patterns associated with loading of the lithosphere are rare [e.g., *Cyr and Melosh*, 1993]. Second, the observed distribution of coronae

is random. *Hieronymus and Bercovici* [2000] predict a regular pattern of volcanoes that are defined by the membrane stresses, the elastic thickness, and the regional stress field.

[6] Hecate chasma was studied in detail by *Hamilton and Stofan* [1996]. They found two primary types of fracture zones, which also have higher concentrations of certain types of coronae. A diffuse fracturing zone is observed in the northwestern region of Hecate, which is dominated by graben and lineaments of indeterminate origin. Coronae in this region have extensive volcanism, are commonly topographic plateaus, and have subradial graben in the interiors. The trough-dominated zone is the main southwest northeast rift branch. It is characterized by highly concentrated normal faults, including those that define graben sets. Coronae in the trough-dominated zone have well-defined annuli, raised rims, and central depressions. Radial lineaments are less pervasive than in the diffuse fracturing zone.

[7] In this paper, we examine the origin and evolution of Hecate and Parga chasmata using new estimates of elastic thickness (T_e) and the apparent depth of compensation (ADC), which is typically interpreted as crustal thickness (Z_c) or lithospheric thickness (Z_L). Specifically, we consider the implications of the similarities and differences of lithospheric structure between the two regions, as well as the relationship between coronae and rifting. The admittance is calculated across each chasma region. This approach produces hundreds of admittance spectra, which are then grouped into classes. We use standard lithospheric loading models to derive lithospheric properties, map out their regional variation, and compare with the distribution of rifts and coronae. We then compare the lithospheric parameter estimated to corona characteristics (e.g., stratigraphic age interpreted from Magellan SAR data for Hecate [*Hamilton and Stofan*, 1996] and Parga chasmata [*Martin et al.*, 2007], amount of volcanism, topographic shape, fracture pattern, and diameter).

2. Methods

2.1. Overview

[8] We produce crustal and elastic lithospheric thickness maps using a multiresolution spatiospectral admittance approach following *Simons et al.* [1997] and spectral classification techniques. To constrain the lithospheric structure, we calculate and map the observed admittance variation across each chasma region (separately) following *Anderson and Smrekar* [2006]. Models are windowed in the same manner as the data. We use classification methods to group spectra by shape and by inference, lithospheric structure. We find that 10 distinct admittance classes (type locales) within Parga and 10 classes (type locales) within Hecate chasma adequately describe the range of admittance spectra shapes. These 20 spectra are then compared to elastic compensation top- and bottom-loading models of predicted admittance to constrain the range of acceptable lithospheric structure.

2.2. Gravity and Topography Data

[9] The admittance is calculated using gravity and topography data obtained by the Magellan spacecraft (1990–1994). The resolution of the gravity field is largely a function of spacecraft altitude but is also influenced by the quality of the signal and the spacing of the tracks. Gravity data were acquired over 98% of Venus at an altitude of 155–220 km,

providing a half wavelength resolution of ~100 km. We use the 180° and order spherical harmonic gravity field described by *Konopliv et al.* [1999]. An approximate measure of the data resolution is provided by the degree strength (the spherical harmonic degree at which the power in the gravity field equals the power in the noise [*Konopliv et al.*, 1999]). The degree strength of the gravity field used here varies from 50 to 100 (half wavelengths of 314–190 km), although this value is likely underestimated by 50% [*Konopliv et al.*, 1999]. Over most of Hecate chasma, the degree strength is between 80 and 100. The larger Parga chasma region varies from 50 to 100, reaching below 50 in a small area in the southwest section of the region studied (see Figure 2). We use the spherical harmonic topography field described by *Rappaport and Plaut* [1994], complete to degree and order 360. Errors in the topography data are disregarded as the topography field is more accurate than the gravity field by more than two orders of magnitude.

2.3. Admittance

[10] The admittance $Q(k)$ is defined as the transfer function between the spectral representation of gravity $G(k)$ and topography $H(k)$:

$$G(k) = Q(k)*H(k) + N(k), \qquad (1)$$

where $N(k)$ is the uncorrelated noise in the data (assumed to be small) and k is the two-dimensional wave number ($2\pi/\lambda$) where λ is the wavelength. Following *Dorman and Lewis* [1970], we assume that the Venusian lithosphere is locally homogeneous and azimuthally isotropic. While various authors have studied the anisotropy of the terrestrial elastic lithosphere [e.g., *Simons et al.*, 2000], simple first-order models (such as those presented here) work well in modeling terrestrial elastic flexure and enable the use of spectral methods.

[11] The admittance spectrum is sensitive to bending of the elastic lithosphere in response to a load from above, below, or both. Admittance is therefore sensitive to elastic thickness (T_e) because elastic thickness controls the surface response of the load [*Watts et al.*, 1980]. The admittance varies depending on whether the topography is supported by the strength of the elastic lithosphere or by subsurface density variations [*Banks and Swain*, 1978; *Forsyth*, 1985].

[12] We calculate the predicted admittance over each chasma using the spatiospectral localization method of *Simons et al.* [1997] that explicitly accounts for the effects of localizing both spectral and spatial information. *Simons et al.* [1997] derive the relationship between the spatial and spectral resolution on a sphere and show the trade-off of spatiospectral information for a window composed of the first lobe of the expansion into spherical harmonics of a boxcar cap. The widths of spatial and spectral windows are inversely related and show that the process of high-resolution spatial windowing requires high-degree spectral information. As end-member examples, a delta function in the spatial domain is described by a constant in the spectral domain, and vice versa; thus, small spatial windows require broad spectral information. The data fields, however, are only reliable up to a maximum Nyquist degree. Using a window of sufficiently small spatial resolution can inadvertently incorporate effectively nondetermined high-degree data coefficients, which
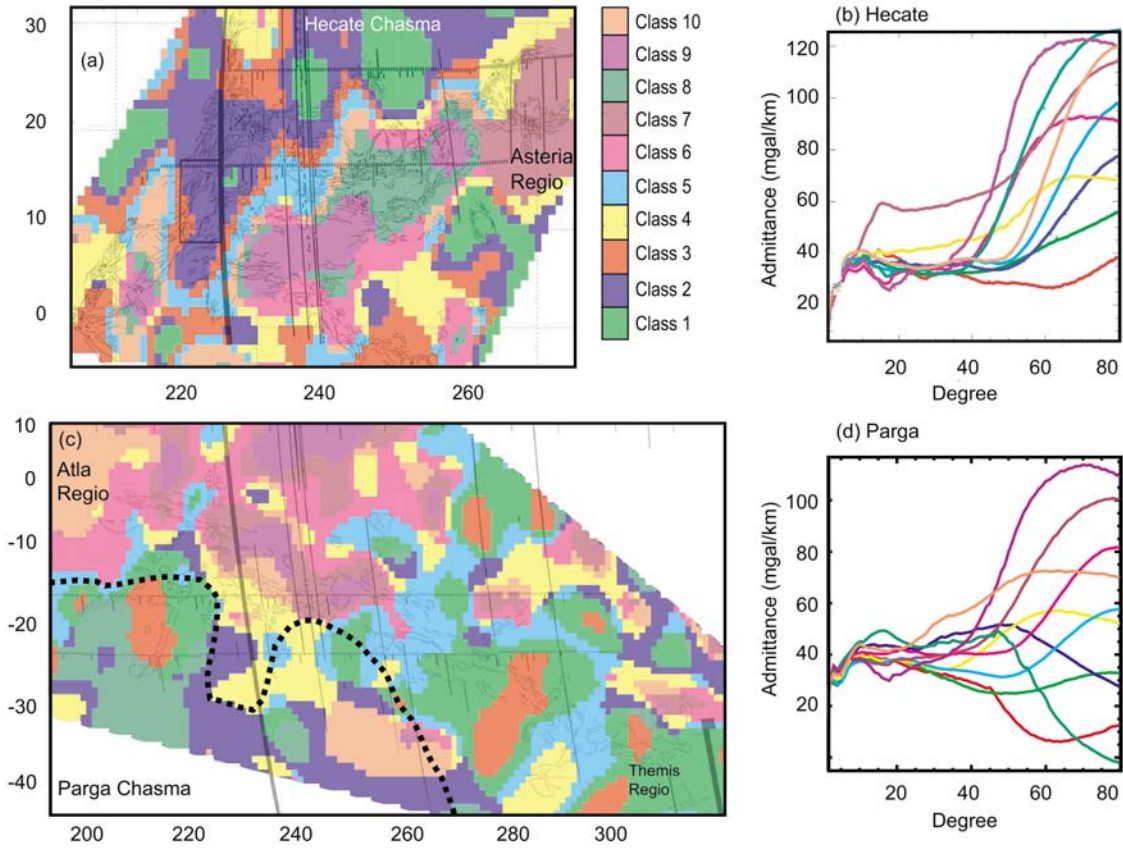
Figure 2. Map locations and admittance spectral classes versus degree and for each of the 10 classes defined for (a, b) Hecate and (c, d) Parga chasmata. The admittance class legend applies to both maps. The admittance classes in Figures 2a and 2c overlay geologic sketch maps for Hecate chasma [*Hamilton and Stofan*, 1996] and Parga chasma [*Martin et al.*, 2007], respectively. In Figure 2c, the dashed line shows the location of the Magellan gravity degree strength of 60 contour. The resolution of the gravity field to the south of this line is too low to be used for admittance studies.

will bias the results. The expression of this effect in admittance, a ratio of equally windowed coefficients, can be insignificant for highly correlated data, as the same biased values are added to both topography and gravity. However, error is likely to be significantly larger as the analysis approaches the degree strength of a field because the magnitude of the bias is inversely proportional to wavelength; hence, at shorter wavelengths, larger amplitude noise is incorporated and dominates the admittance value.

[13] For the spherical harmonic window chosen by *Simons et al* [1997], the parameter, f_s, controls spatial or spectral dominance for all spherical degrees. Following *Simons et al* [1997], maximum spectral resolution (or the shortest wavelength that can be resolved within the chosen spherical harmonic window) is

$$\lambda_{spectral} = \frac{2\pi R}{\sqrt{L_{nyq}(L_{nyq}+1)}}, \quad (2)$$

where R is the radius of Venus (~6052 km) and the Nyquist degree is

$$L_{nyq} \cong L_{obs} \cdot \frac{f_s}{(f_s+1)}. \quad (3)$$

To maximize the spatial resolution of local features, we set $f_s = 2$.

[14] The maximum calculated degree strength for the gravity field of Venus (L_{obs}) is ~120°, and much of the planet has values exceeding 80°. Because L_{obs} increases by 50% due to the underestimation of the error (Konopliv, personal communication, 2000, 2005) and for $f_s = 2$, L_{nyq} is equal to $2/3 L_{obs}$, we can utilize the resolution of the data out to degree 80 in most regions. This approach maximizes the spatial resolution and represents an appropriate compromise for the range of resolution in the field.

[15] After convolving the topography and gravity field harmonics with the appropriate window coefficients to achieve the desired spatial or spectral resolution, the admittance is calculated by dividing the cross covariance of gravity and topography by the cross covariance of topography with topography. Each cross covariance is calculated for all of the harmonics within the window associated for each degree up to the Nyquist degree of the most resolution-limited spherical harmonic field. The admittance centered at a point location on the surface is [*Simons et al.*, 1994, 1997]

$$F_1(\Omega) = \frac{\sigma^2_{\Psi\Gamma}(\Omega)}{\sigma^2_{\Psi\Psi}(\Omega)}, \quad (4)$$

where F_1 is the admittance, Ω is the region of the surface in a spherical domain, and $\sigma^2_{\Psi\Gamma}(\Omega)$ and $\sigma^2_{\Psi\Psi}(\Omega)$ are the cross covariance of the topography to gravity ($\Psi\Gamma$) and topography to topography ($\Psi\Psi$) fields. Error is calculated from the correlation of the spherical harmonic fields. More detail can be found in the work of *Simons et al.* [1997].

2.4. Global Admittance Map

[16] The observed global admittance is calculated using the method described by *Anderson and Smrekar* [2006] and *Smrekar et al.* [2003]. A global observed admittance map is calculated by moving the center point of the spherical cap by 1° in latitude and longitude, creating an admittance spectrum at each of 360 × 180 points. While there is considerable overlap in the spectral content for two adjacent regions, the short-wavelength information changes smoothly due to the spectral nature of the data. Relative RGB color intensities are then assigned to the relative admittance values at three different wavelengths (red = 475 km, green = 580 km, blue = 750 km). The resulting map represents a classification scheme that highlights short-wavelength variations in the observed admittance. The observed admittance is variable, consistent with geologic changes across the planet.

[17] From the global admittance map, the admittance across the Hecate and Parga chasmata regions is classified following the method used by *Smrekar et al.* [2003], in which similar admittance spectra are identified, grouped, and averaged for each chasma region. The total spectra are thereby reduced to a limited set of representative classes across each chasma region, each with a mean spectrum and the standard deviation from that mean spectrum. An iterative self-organizing (ISODATA) classification method is used to calculate class means evenly distributed in the data space and then iteratively cluster pixels using minimum distance techniques [*Tou and Gonzalez*, 1974; ENVI Users Guide, 1999]. Classes were defined using points with degree strength of >80 to avoid creation of classes derived from low-resolution data. Ten classes across each rift were sufficient to represent all of the observed spectra (with a degree strength of >80 and an RMS error over a range of degree strength of less than 10 mgal/km, a value appropriate for the mean error in the resulting admittance [*Smrekar*, 1994]). Next, all 20 of the observed classes were compared to the average of the derived classes, and the location of the most similar observed spectra ("type locales") were recorded. Each of the 20 type locale classes is then compared with compensation models, assuming an elastic lithospheric layer to calculate lithospheric properties.

2.5. Compensation Models

[18] Interpretation of gravity data is fundamentally nonunique in the absence of additional constraints. However, on Earth, simple two-layer mechanical models of the lithosphere provide acceptable first-order interpretations of the lithosphere [*McNutt*, 1983; *Forsyth*, 1985]. As such, we use two simple top- and bottom-loading mechanical models to interpret the observed admittance functions of the Venusian lithosphere.

[19] We assume that the lithosphere comprises two laterally homogenous layers: crust of thickness Z_c and mantle lithosphere of thickness Z_L, which are loaded by a harmonically varying topography, either at the surface (top loading) or at a compensation depth below the crust-mantle interface (bottom loading). The lithosphere is assumed to be in static equilibrium with stresses supported by elastic flexure of the uppermost elastic layer, thickness T_e. As T_e approaches 0, we obtain the limit of local isostatic compensation. We compare the predicted admittance from both top- and bottom-loading models to the observed admittance. Certainly, these two layers, a crustal layer (Z_c) and a thermal lithosphere (Z_L), exist on Venus. However, there may well be other density variations, such as a basalt-eclogite transition, that contribute to lithospheric compensation and the gravity signature. Thus, we report the Z_c and Z_L results derived from these basic compensation models but recognize that they are, in fact, apparent depths of compensation and are not necessarily direct estimates of crustal and thermal lithospheric thickness.

[20] The standard transfer function between free air gravity anomalies and topography for loading of the elastic lithosphere from above (top loading) is given by *Banks and Swain* [1978]:

$$Q_T(k) = 2\pi\rho_c G\left[1 - e^{-kZ_c}/\left(1 + Dk^4/\Delta\rho g\right)\right], \qquad (4')$$

where $k = \sqrt{l(l+1)}/R$ is the horizontal wave number, ρ_c is the crustal density, G is the gravitational constant, Z_c is the thickness of the crust, g is surface gravity (8.87 m s^{-2}), and $\Delta\rho$ is the density contrast at the crust-mantle boundary. Top-loading models are a function of crustal and elastic thickness (Z_c and T_e).

[21] In all models, crustal and mantle densities of 2800 and 3300 kg/m^3 are assumed, respectively. The flexural rigidity (D) is defined by

$$D = \frac{ET_e^3}{12(1-\nu^2)}, \qquad (5)$$

with nominal parameter values of E, Young's modulus (10^{11} Pa), and ν, Poisson's ratio (0.25).

[22] Both loading signatures imply that the topography is at least partially compensated by flexure of the elastic lithosphere. Local isostasy ($D \to 0$) indicates that the region is compensated by variations in the layer thickness that balances the surface topography. Under isostatic conditions, the admittance is

$$Q_T(k) = 2\pi\rho_c G\left(1 - e^{-kZ_c}\right). \qquad (6)$$

From *McNutt* [1983], *Anderson and Banerdt* [2000] derive the spherical harmonic representation of the admittance resulting from a load at depth (bottom loading):

$$Q_N = 2\pi G\left[\rho_c + (\rho_m - \rho_c)e^{-kZ_c} - \left((Dk^4 + \rho_m g)/g\right)e^{-kZ_L}\right], \quad (7)$$

where ρ_m is the mantle density. This bottom-loading equation includes a crustal interface and a second density interface at depth Z_L below the crust mantle boundary. Apparent depth of compensation (Z_L) defines the depth above which the mass of the topography is balanced by a compensating mass at depth. As crustal thickness cannot be constrained independently of the apparent depth of compensation using only gravity and topography data, we assume a crustal thickness of 30 km

(following previous estimates of the mean thickness of the crust [e.g., *Grimm and Hess*, 1997]) for the bottom-loading model and use the model to constrain elastic thickness and apparent depth of compensation (Z_L). Using a larger crustal thickness value results in a larger value of apparent depth of compensation. Bottom-loading models are a function of the depth to the load in the lithosphere (Z_L) and assume a density anomaly at depth, such as a mantle upwelling, which displaces the elastic lithosphere [*McKenzie and Bowin*, 1976; *McNutt*, 1983; *Forsyth*, 1985; *McNutt*, 1988; *Sheehan and McNutt*, 1989; *Zuber et al.*, 1989; *Smrekar*, 1994; *Smrekar et al.*, 1997].

[23] A variety of processes can cause the elastic lithosphere to be loaded from above or below. A bottom-loading signature may imply that a low-density mass (e.g., a plume) is pushing up on the base of the lithosphere to create a topographic high. Alternatively a high-density mass (or downward flow in the mantle) pulls the lithosphere down creating a topographic low. A region exhibiting a top-loading signature may be explained by a surface mass (e.g., a volcano) depressing the original topography as the elastic plate flexes. If the load is interpreted as a mantle plume, the inferred depth to the load (or the effective lithospheric thickness) is a function of lithospheric and mantle viscosity [e.g., *Robinson and Parsons*, 1988; *Kiefer and Hager*, 1992]. In many cases, however, there is no obvious surface load.

[24] Top- and bottom-loading elastic flexure signatures can also be mimicked by dynamic processes in a viscous mantle. *Smrekar et al.* [1997] show that a large-scale mantle plume can also produce a top-loading signature. Dynamic stress associated with flow in the mantle and static stress associated with variations in crustal layer thickness may only be partially supported by elastic strain in the lithosphere. Despite these complications, these first-order models are effective in describing elastic flexure on Earth [e.g., *McNutt*, 1983]. In the absence of other constraints, we apply these models to interpret the observed admittance functions of Hecate and Parga chasmata on Venus.

2.6. Estimating Lithospheric Parameters

[25] An automated routine calculates the best fit between the observed average admittance and the compensation model over a specified wavelength range (generally $40 \le l \le 80$). The upper bound of the range depends on the local degree strength across each chasma. The lower bound (degree 40) is chosen following *Nimmo and McKenzie* [1996], who suggest that any gravity signal at wavelengths longer than 1000 km cannot be due to elastic effects. Model fits are iteratively compared to the observed spectra, and the minimum misfit found by varying T_e and Z_c by increments of 5 km and Z_L by increments of 10 km. The range of T_e values considered for top loading ($0 < T_e < 125$ km) and bottom loading ($0 < T_e < 100$ km) was chosen to incorporate the range of T_e estimates obtained from a variety of previous studies [e.g., *Sandwell and Schubert*, 1992a, 1992b; *Johnson and Sandwell*, 1994; *Anderson and Smrekar*, 2006]. The range of crustal thickness values considered ($0 < Z_c < 100$ km) was chosen to incorporate the range of Z_c values obtained from previous theoretical, geodynamic, and gravity studies reviewed by *Grimm and Hess* [1997]. The range of Z_L values considered for bottom loading is between $30 < Z_L < 200$ km.

2.7. Error Analysis

[26] Several factors contribute to the uncertainty in the inferred flexural parameters. In this analysis, noise is represented as scatter in the admittance and is not considered explicitly. Recent studies address the importance of method biases on estimation of T_e [*Lowry and Smith*, 1994; *Simons et al.*, 2000]. A significant source of uncertainty arises from the lack of independent constraint on crustal thickness and density. These uncertainties are accounted for following the approach adopted by *McKenzie and Fairhead* [1997], corresponding to 1.5 times the observed RMS error in the average admittance. The observed error in the spatiospectral spectrum is defined as the average error in the spectral classes used to represent the region and quantify the RMS error contained within a class. For each class, we assume that the variation in admittance values in the target region is representative of the uncertainty in admittance and is equal to 1.5 times the standard deviation about the mean:

$$\mathrm{RMS}_l = \frac{1}{N_{\mathrm{ADM}}} \left[\sum (x_l - \mu)^2 \right]^{\frac{1}{2}}, \qquad (8)$$

where μ is the average class admittance, x_l is the admittance at degree l, and N_{ADM} is the number of admittance signatures averaged over.

[27] An average admittance error for each class is defined by

$$\mathrm{RMS} = \frac{1}{N_L} \sum_l \mathrm{RMS}_l, \qquad (9)$$

where N_L is the number of degrees for which a compensation model is fit.

2.8. Coherence

[28] Numerous studies have addressed the question of the importance of subsurface loading on estimates of T_e. *Forsyth* [1985] found that internal loading has an important effect on values of the admittance and argued that the effect of variation of f (the ratio of the internal to the surface load) on estimated values of T_e could be reduced using the coherence between Bouguer gravity and topography. Coherence provides a measure of the statistical relationship between gravity and topography and is relatively insensitive to the effects of top and bottom loading and to errors in the depth of subsurface loading [*Forsyth*, 1985]. The method generally assumes that top- and bottom-loading processes are uncorrelated. Note that, except for a few isolated regions, gravity data for Venus does not have adequate resolution to permit coherence studies.

2.9. Results

[29] The derived lithospheric parameters for each class in Hecate and Parga chasmata are provided in Table 1. The admittance class spectra and the distribution of all 20 classes are shown in Figure 2. The model fits and errors for Parga chasma are shown in Figures 3 and 4, respectively. Hecate chasma admittance model fits are shown in Figure 5, with errors in Figure 6. With the exception of one class (class 9), all Parga classes were only fit by a bottom-loading model. The top-loading model results were found to have average error values greater than 20 mgal/km and were eliminated. Class 9
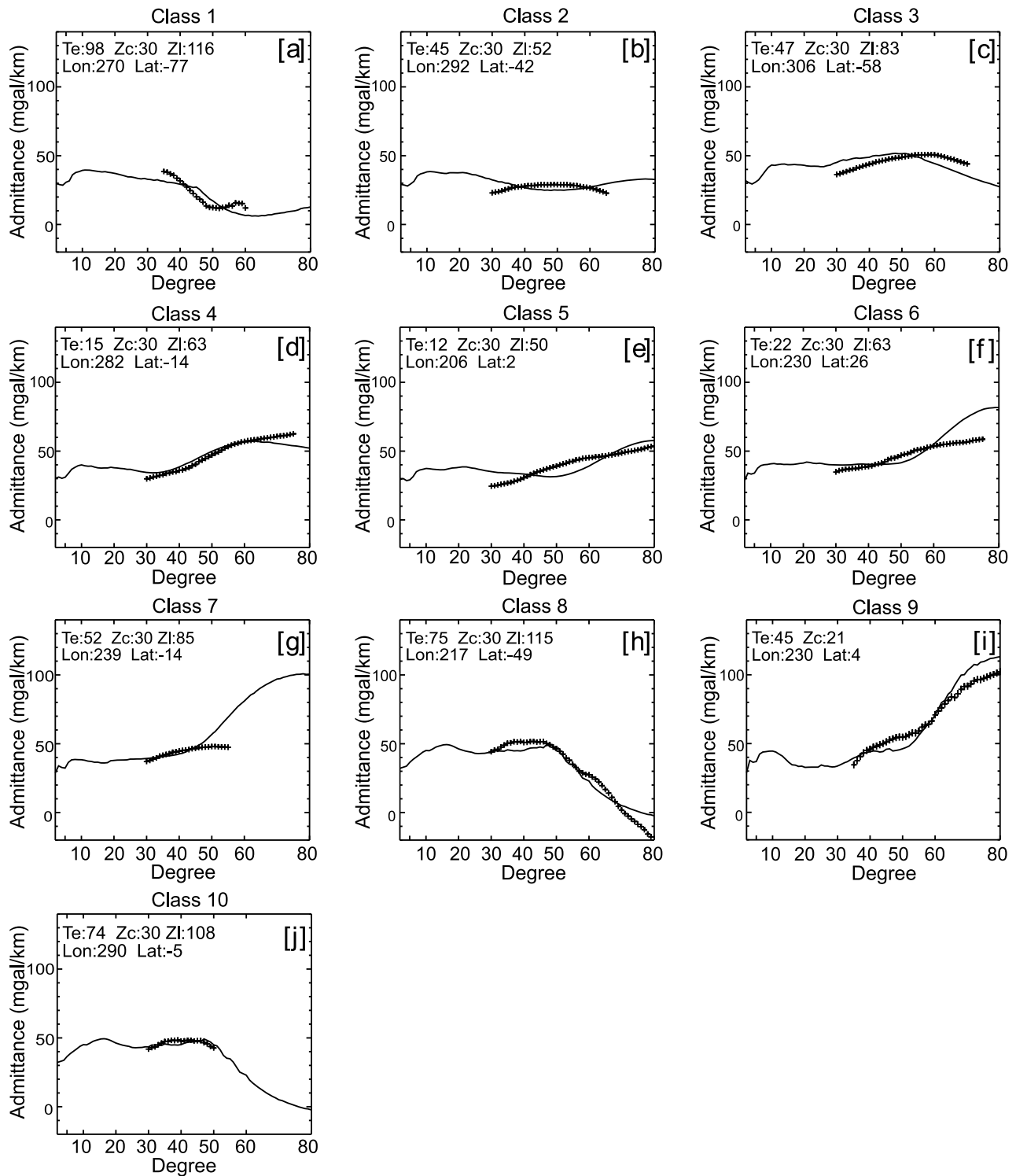
Figure 3. (a–j) Spatiospectral admittance spectra (solid lines) for 10 classes representing admittance signatures across Parga chasma. Best fit theoretical admittance functions are shown as crosses. The best fit values of T_e and Z_L (or Z_c in the case of the single top-loading model in Figure 3i) are displayed in the top left.

was only fit by a top-loading model. The admittance classes across Hecate showed greater variation in best fit compensation model. In this case, classes 1 and 4 were better fit by bottom-loading compensation models. Classes 2 and 3 admittance spectra were fit by either a top- or bottom-loading

compensation model producing similar elastic thickness estimates. Class 7 was fit by either a top- or bottom-loading model with widely varying elastic thickness (and Z_c or Z_L) estimates; however, the bottom-loading error was better constrained. Classes 5, 6, and 8–10 were only fit by a top-
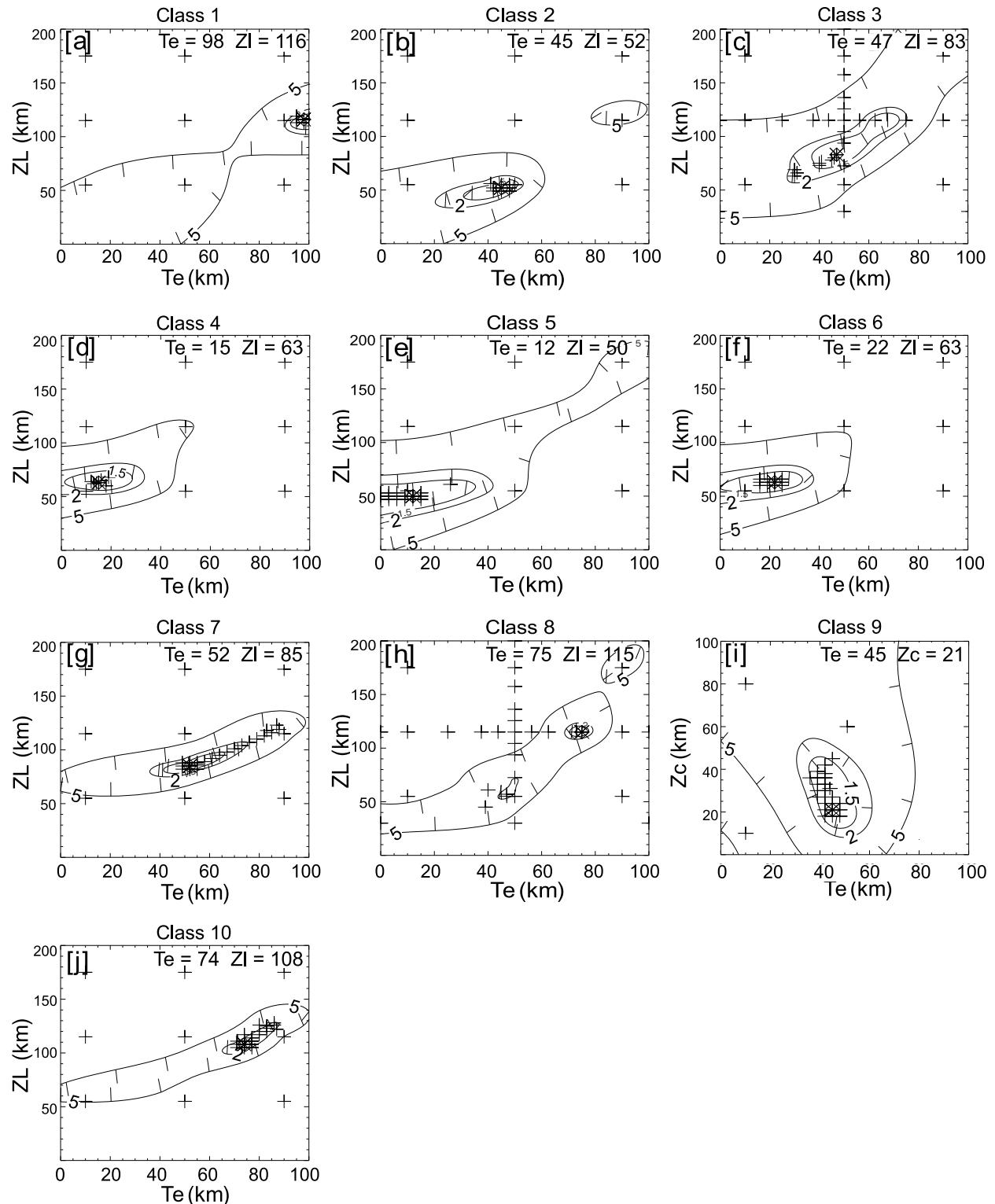
Figure 4. (a–j) RMS model misfits (units: mgal/km) are shown for 10 Parga class models in the Z_L-T_e plane (bottom-loading models) and the Z_c-T_e plane (in the case of the single top-loading model fit shown in Figure 4i). Cross marks the location of the best fit value. The RMS misfit in each plot is normalized by the RMS variation in the observed admittance spectra. Allowable ranges for T_e, Z_c, and Z_L are based on an RMS misfit of 1.5 times the estimated RMS admittance error.
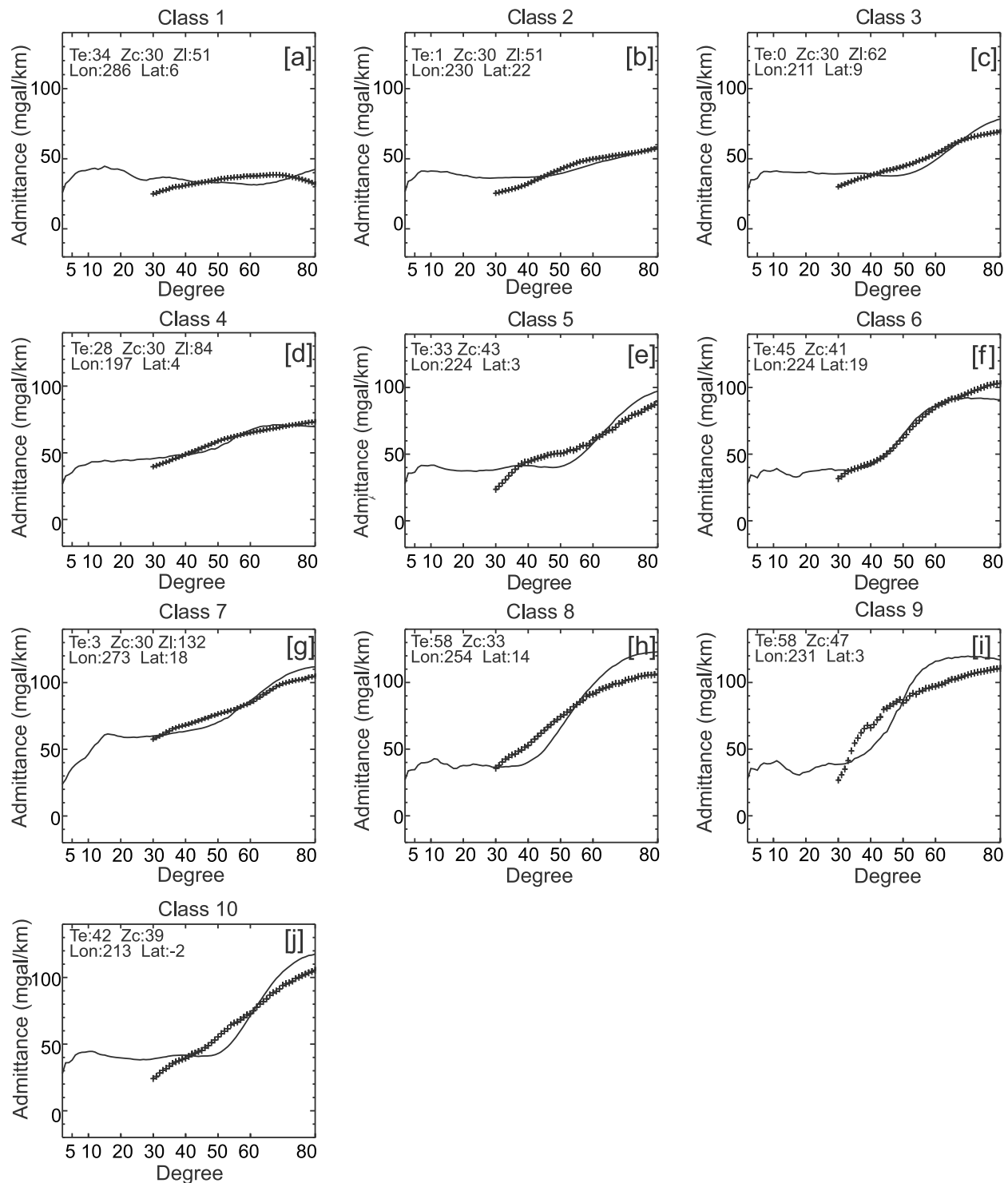
Figure 5. (a–j) Spatiospectral admittance spectra (solid lines) for 10 classes representing admittance signatures across Hecate chasmata. Best-fit theoretical admittance functions are shown as crosses. Due to improved gravity data resolution at Hecate, each class was fit across the range of 40°–80°. The best fit values of T_e and Z_L (or Z_c in the case of top-loading models in Figures 5e, 5f, 5h–5j) for classes fit by a bottom-loading model are shown in the top left.
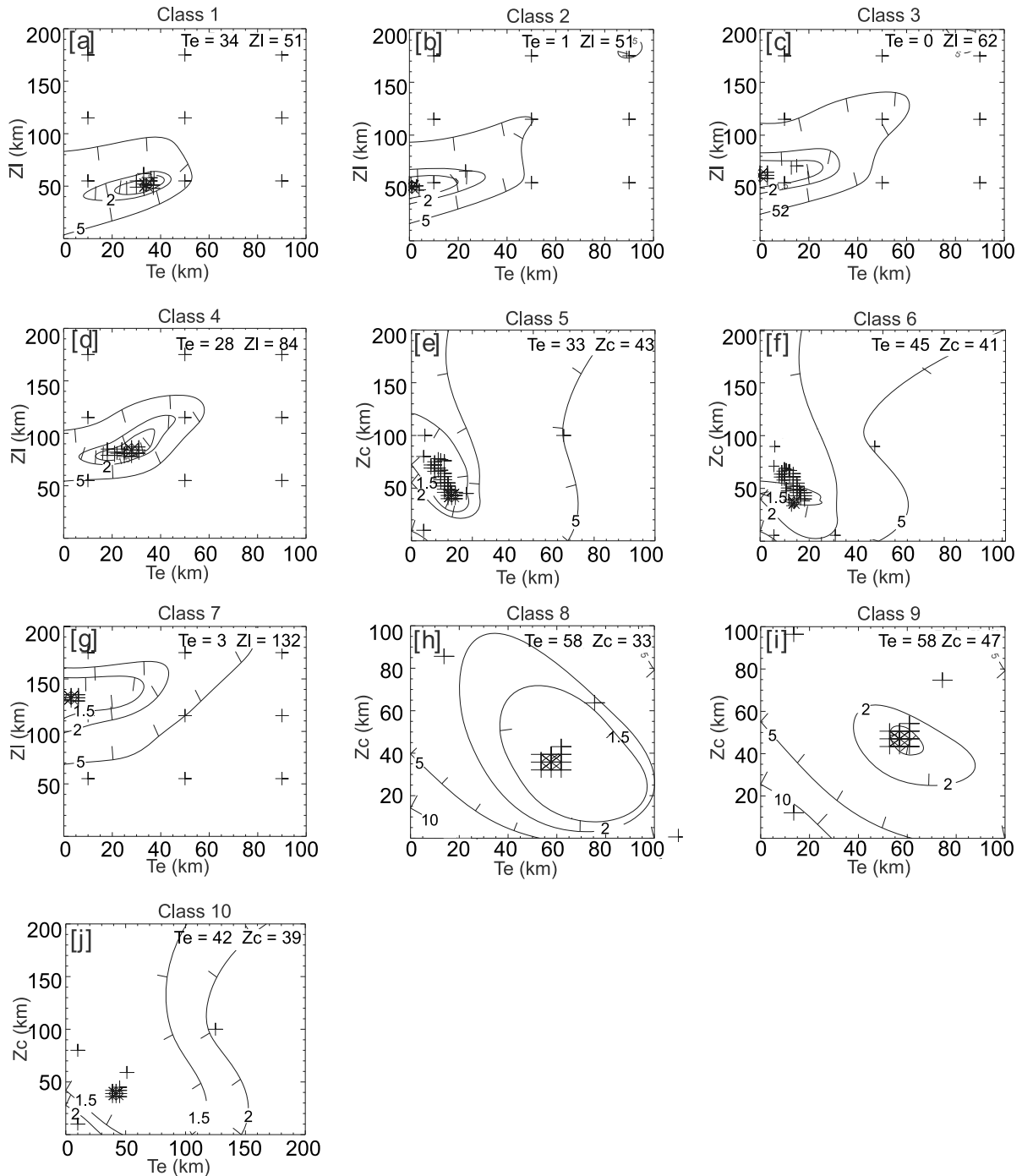
Figure 6. (a–j) RMS model misfits (units: mgal/km) are shown for 10 class models in the Z_L-T_e plane (in the case of bottom-loading models in Figures 6a–6d, 6g) and the Z_c-T_e plane (in the case of top-loading models in Figures 6e, 6f, 6h–6j). Cross marks the location of the best fit value. RMS misfit in each plot is normalized by the RMS variation in the observed admittance spectra. Allowable ranges for T_e, Z_c, and Z_L are based on an RMS misfit of 1.5 times the estimated RMS admittance error.

loading model. The corresponding bottom-loading models had model fit errors that were too large (>13 mgal/km) to adequately represent the observed admittance.

[30] For Parga, the range of best fit elastic thickness values is 12–98 km, with a mean and standard deviation of 48 ± 28 km. The apparent depth of compensation ranges from 21 to 116 km, with a mean and standard deviation of 76 ± 31 km. Only one class was best fit by a top-loading model that produced a crustal thickness of 21 km. For Hecate, the range of best fit elastic thickness values is 0–58 km, with a mean and standard deviation of 30 ± 22 km. The apparent depth of compensation ranges from 51 to 132 km, with a mean and

Table 1. Fits to the 10 Spectral Classes for (a) Hecate and (b) Parga Chasmata[a]

Class	Best Fit Load	Best Fit T_e (km)	Min (km)	Max (km)	Group	Best Fit Z_c or Z_L (km)	Min (km)	Max (km)	RMS (l)	Group
					Hecate					
1	BL	34	21	41	med	51	41	60	5.5	med
2	BL	1	1	19	v. low	51	40	61	4.5	med
3	BL	0	0	25	v. low	62	50	76	5.3	med
4	BL	28	13	29	med	84	74	104	2.9	high
5	BL	33	0	47	med	43	**28**	**120**	3.6	low
6	BL	45	39	50	high	41	37	47	0.4	low
7	BL	3	0	33	v. low	132	112	152	4.8	v. high
8	BL	58	**42**	**96**	high	33	**10**	**69**	2.7	low
9	TL	58	57	63	high	47	45	51	1.1	low
10	BL	42	**30**	**116**	high	39	**0**	**60**	6.6	low
					Parga					
1	BL	98	92	99	high	116	106	121	1.6	v. high
2	BL	45	30	51	med	52	40	59	0.8	med
3	BL	47	36	72	med	83	**69**	**121**	1.2	high
4	BL	15	1	28	low	63	55	74	3.2	med
5	TL	12	1	35	low	50	32	65	2.3	med
6	TL	22	0	33	low	63	53	73	1.4	med
7	BL	52	41	66	med	85	78	97	0.7	high
8	TL	75	70	77	high	115	110	120	3.2	v. high
9	TL	45	35	55	med	21	12	47	2.1	v. low
10	TL	74	71	74	high	108	104	108	1.1	v. high

[a]Top and bottom loads (TL or BL, respectively) are fit to each spectrum. The solution with the smaller error is used. The minimum and maximum values are based on an error ratio of 1.5 (Figures 4 and 6). Classes that have a difference between the maximum and minimum values in excess of 50 km are least reliable and are in bold. See text for discussion of errors. Crustal thickness Z_c for top-loading fits or compensation depths Z_L for bottom loads are classified into groups of very low (<25 km), low (25–45 km), medium (45–75 km), high (75–100 km), and very high (>100 km) based on the best fit values. Elastic thicknesses are classified into very low (<10 km), low (10–40 km), medium (40–70 km), and high (>70 km) groups on the basis of the best fit values.

standard deviation of 76 ± 34 km. Crustal thicknesses between 33 and 47 km were inferred, with a mean and standard deviation of 40 ± 5 km.

2.10. Error Estimates

[31] The error plots shown in Figures 4 and 5 illustrate the range of acceptable lithospheric parameters for the same 20 classes with the best fit values of T_e, Z_c, and Z_L reported in Table 1. Following *McKenzie and Fairhead* [1997], the acceptable ranges for T_e, Z_c, and Z_L are those for which the RMS misfit is within 1.5 times the estimated RMS variation of the observed admittance. For bottom-loading models, the mean uncertainty for T_e is 22 km and that for Z_L is 23 km. Top-loading models display a mean uncertainty of 37 km for T_e and 43 km for Z_c. Some classes are not especially well fit, as seen by the large range of allowable values (Table 1). These classes are typically transitional between one class and another with quite different lithospheric values. When the lithospheric structure is nonisotropic, fits to the admittance will not yield well-constrained values. In other classes with large errors, the admittance curves are very steep and difficult to fit, possibly indicating dynamic behavior.

2.11. Lithospheric Structure

[32] Estimates of elastic thickness obtained from admittance studies for a variety of Venusian features [*McKenzie and Nimmo*, 1997; *Simons et al.*, 1997; *Barnett et al.*, 2000; *Smrekar and Stofan*, 2003] range from 10 to 65 km. Consistent with those earlier studies, T_e estimates found here range between 0 and 98 km.

[33] Of the classes examined in this paper, 5% are best fit with an elastic thickness of 0 km. A further 20% have a best fit elastic thickness of less than 20 km and include 0 km in their range of uncertainty. Low T_e values may be interpreted as

implying high heat flow and thin elastic lithosphere. Alternatively, they may indicate isostatic compensation, implying that the topography is supported by subsurface density variations, typically interpreted as crustal thickness variations. In this interpretation, loading stresses in the elastic lithosphere have relaxed, and little if any of the load is compensated by elastic flexure or by dynamic processes. In addition to density interface displacements, isostatic compensation may also result from temperature differences or compositional variation.

[34] If the five classes with isostatic or near-isostatic signatures are removed, the range of T_e for top-loading models is 22–74 km. A top-loading fit is more influenced by power in the short wavelengths of the admittance functions and assumes no contribution from strength in the mantle [*Forsyth*, 1985; *Petit and Ebinger*, 2000]. Such models may therefore be biased toward smaller values of T_e. Bottom-loading models show a larger range of T_e values (0–98 km). Terrestrial investigations that have examined both compensation models also indicate larger values for bottom loading [e.g., *Petit and Ebinger*, 2000]. Differences in analysis methods may also influence estimates of elastic thickness [see *Petit and Ebinger*, 2000].

[35] The range of crustal thickness values obtained from the five classes best fit with a top-loading model (21–63 km) includes the range of 20–50 km determined in a variety of Venusian gravity studies for different geologic features, as summarized by *Grimm and Hess* [1997]. Significantly larger values of compensation are interpreted as apparent depth of compensation rather than crustal thickness.

[36] In a dynamic mantle, the apparent depth of compensation is strongly dependent on lithospheric viscosity and mantle structure [*Moresi and Parsons*, 1995; *Smrekar et al.*, 1997] and is not simply interpreted as the depth to a thermal

anomaly at the base of the lithosphere. Estimates of Z_L can, however, be used to compare relative depths of compensation between classes. The average Z_L value we obtain for classes interpreted using a bottom-loading model is 79 km and ranges from 32 to 152 km. Some variation in Z_L may be due to the range of dynamic processes in chasma formation, but the range is similar to those obtained in previous studies of other geological structures [*Brian et al.*, 2004; *Herrick et al.*, 2005; *Anderson and Smrekar*, 2006; *Grindrod et al.*, 2006]. Smaller values of Z_L of less than 50–75 km are probably best interpreted as crustal thickness. Variations in the density structure from what is assumed in our models will cause errors in estimates of Z_c or Z_L. For example, a dense eclogite would cause compensation depths to be overestimated. We refer to estimates of Z_c or Z_L from top- or bottom-loading models, respectively, as the apparent depth of compensation (ADC) to emphasize that derived values may be affected by processes other than those modeled.

[37] Although 10 classes are defined for both Parga and Hecate chasmata, some classes are similar in shape and lithospheric properties. For example, Hecate classes 6 and 10 have similar best fit crustal and elastic thickness, although class 6 has smaller error bars. At Hecate, most occurrences of classes 3, 5, and 10 are transitional from one class to another in most locations. Additionally, some classes occur in the surrounding plains or other geologic provinces and are thus not part of the rift story. To provide a comparison between the two regions, we group the classes for Parga and Hecate based on their lithospheric properties into those with very low, low, medium, and high elastic thickness and very low, low, medium, high, and very high crustal thickness or apparent compensation depth (see Table 1). Grouping into these more general classes is also consistent with the limits of the data resolution and associated methods. Although some groups could be combined based on the allowable fits to T_e or Z_c, we have kept some of the finer distinctions because of their unique geologic associations. For example, the very low T_e group is composed of Hecate admittance classes 2, 3, and 7. Classes 2 and 3 are very similar and define the northwestern portion of Hecate chasma. Class 7 is unique to Asteria Regio, which has been previously classified as a hot spot [*Smrekar and Phillips*, 1991]. The very low crustal thickness class occurs only in Parga and is associated with the largest coronae in Parga: Atete and Maram.

3. Discussion

3.1. Rifting and Lithospheric Structure

[38] Both the ranges (Table 1) and spatial distributions of elastic thickness and apparent depth of compensation differ between Hecate and Parga chasmata (Figure 7). The elastic thickness and apparent depths of compensation are, on average, smaller at Hecate chasma than at Parga chasma. The difference in the spatial distribution of admittance classes and the associated elastic thickness and apparent depth of compensation is striking. We further note that few classes have the combination of thin elastic thickness, large compensation depths, and bottom-loading signatures consistent with their being supported by an active plume.

[39] Hecate chasma appears to be a relatively well-organized rift system, with an admittance signature that is distinct from the surrounding plains. The admittance signature is strongly correlated with the location of the main southwest northeast and the major northwest segment of the rift. The ADC values in the main trend of the rift are low (~30–50 km), and the elastic thickness is high (~40–60 km). These values are consistent with significant extension. However, examination of the fracture systems does not imply substantial extension. This subject will be discussed in detail in a follow-on paper [*Smrekar et al.*, 2009]. In regions where the crust has been significantly thinned and the mantle is closer to the surface, elastic thickness will be large and the ADC relatively shallow. The northwestern segment has low-moderate (~50 km) ADC values and low elastic thickness (~0 km). The low elastic thickness and the larger ADC value suggest that this region may be currently extending or has experienced less extension.

[40] Further, these two segments of the rift correspond to regions with distinct rift morphologies. *Hamilton and Stofan* [1996] define a diffuse fracturing zone that is dominated by graben and indeterminate lineaments, which they interpret to indicate a broad tectonic accommodation of deformation. The second type of region is a trough-dominated zone, where fractures are clearly normal faults, including graben sets. The northwest branch is characterized by diffuse fracturing. Branches on the western and southern margins often have diffuse fracturing as well. Many of these branches vary in elastic and crustal thickness along their lengths. The trough-dominated region corresponds to the main branch of the rift, which has high elastic thickness and low Z_L. In a companion paper, we examine rifting at Hecate chasma using a simple model of lithospheric extension and find good agreement with the geology [Smrekar et al., 2009].

[41] At Parga, there is no such obvious association between rift segments and lithospheric properties. Most of the rift has an intermediate elastic thickness and ADC. However, the rift is not distinct from the surrounding plains, as is much of Hecate chasma. On one segment of the rift, which is bounded by the two largest coronae (Maram at 7.5°S, 221.5°E and Atete at 16°S, 243.5°E, both with diameters of ~600 km), an alignment of lithospheric properties is observed. Even within this segment, which is essentially composed of gravity classes 7, 9, and 10, there are significant variations in the associated lithospheric properties. Classes 7 and 10 have somewhat similar values, with a combined range of elastic thickness of ~50–75 km and a range of ADC of ~85–110 km. In contrast, class 9, which in Parga appears only at Atete and adjacent to Maram coronae, is very unusual with an ADC of 21 km and an elastic thickness of 45 km.

[42] Themis Regio, at the southeastern end of Parga chasma, has a distinct signature, with thin elastic lithosphere (~10–15 km) and moderate ADC (~50–65 km). This ADC is relatively low compared with large volcanic rises such as Beta and Atla regions [e.g., *Stofan and Smrekar*, 2005, and references therein] and is typical of hot spot rises with numerous coronae, such as Central and Eastern Eistla regions [*Smrekar and Stofan*, 1999]. These shallow ADCs have been interpreted as reflecting numerous shallow plumes on the scale of the coronae rather than a broad-scale plume on the scale of the topographic rise [*Smrekar and Stofan*, 1999].

3.2. Coronae and Lithospheric Structure

[43] In Hecate chasma, *Hamilton and Stofan* [1996] found that some corona characteristics correlated with the rift
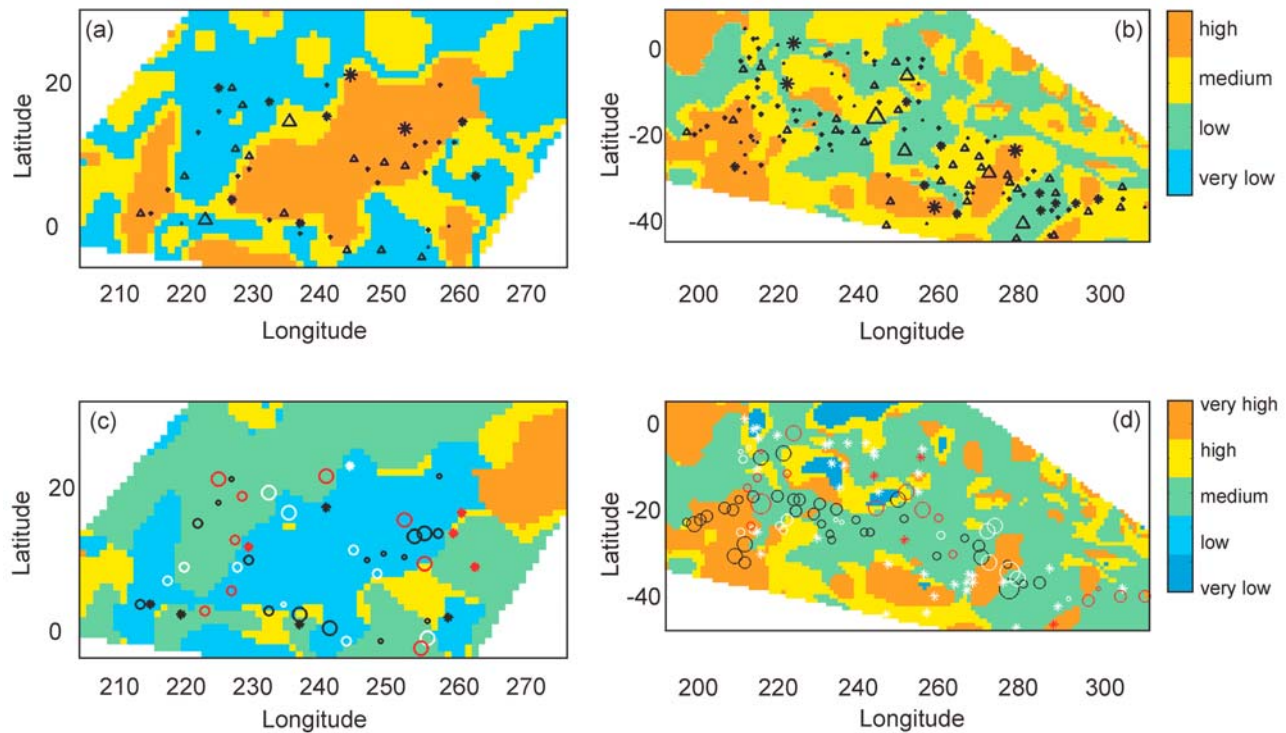
Figure 7. Maps of (a, b) the distribution of elastic thickness and (c, d) crustal thickness (Z_c) or compensation depth for (a, c) Hecate and (b, d) Parga chasmata. The legends use consistent kilometer ranges for T_e between Parga and Hecate chasmata, so that each plot does not necessarily contain each class. The same is true for Z_c maps. Refer to Table 1 and Figures 2 and 3 for specific class values and ranges. Coronae as a function of diameter are also shown on Figures 7a and 7b: small triangles (<100 km), small stars (100–200 km), medium triangles (200–300 km), medium stars (300–400 km), large triangles (400–500 km), large stars (500–600 km), and extra large triangles (600–700 km, only Atete Corona in Parga chasma). The age of the coronae relative to the rift is shown in Figures 7c and 7d, where the oldest coronae have the smallest symbol size and the youngest coronae have the largest symbols. Those that lie off the rift are shown as stars. The amount of volcanism is also denoted in Figures 7c and 7d by color: low (black), medium (white), and high (red).

fracture type. As fracture type correlates with lithospheric structure in broad regions of the rift, these corona characteristics are also correlated. Specifically, *Hamilton and Stofan* [1996] found that many of the coronae in diffuse fracturing regions have extensive volcanism, are defined as topographic plateaus, and have subradial graben in the interiors. These trends hold well for the northwest branch described by *Hamilton and Stofan* [1996] but break down in the more complex western and southern sections of the rift. Many coronae in the trough-dominated zone have well-defined annuli, raised rims, and central depressions. Radial lineaments are less pervasive.

[44] These distinct zones in Hecate chasma correlate well with lithospheric structure. The northwest region has very low elastic thickness (~0 km) and a moderate ADC (~50 km). If we interpret the elastic thickness to indicate higher thermal gradients and thinner thermal lithosphere, this would be consistent with large amounts of volcanism. The preference for coronae with positive topography in the fracture-dominated zone would also be consistent with the ability of plumes or zones of decompression melting to rise relatively easily in a thin lithosphere. The central region with the main trough has relatively high elastic thickness (40–60 km) and

low ADC (30–50 km). The admittance curves in this region are very steep (see classes 7–10 in Figure 2b). *Smrekar and Stofan* [1999] have previously interpreted such a signature as predominantly dynamic and possible evidence of lithospheric delamination. This is consistent with the observation that about half of the coronae are topographic depressions in this area, although positive relief features can also form above sites of delamination via isostatic rebound [*Hoogenboom and Houseman*, 2006]. The presence of a dense mantle layer near the surface in an area of high heat flow would certainly favor delamination [*Elkins-Tanton et al.*, 2007]. The ADC throughout Hecate is low to medium and suggests compensation near the base of the crust rather than by an active mantle upwelling.

[45] The population of coronae at Parga chasma is not as well organized over broad regions, although there are rift segments that have predominately topographically positive or negative coronae. *Martin et al.* [2007] find depressions along their rift segments 13 and 14 and coronae with positive relief along segments 1, 6, and 11. However, these rift segments do not have distinct signatures in the admittance and thus their lithospheric properties.
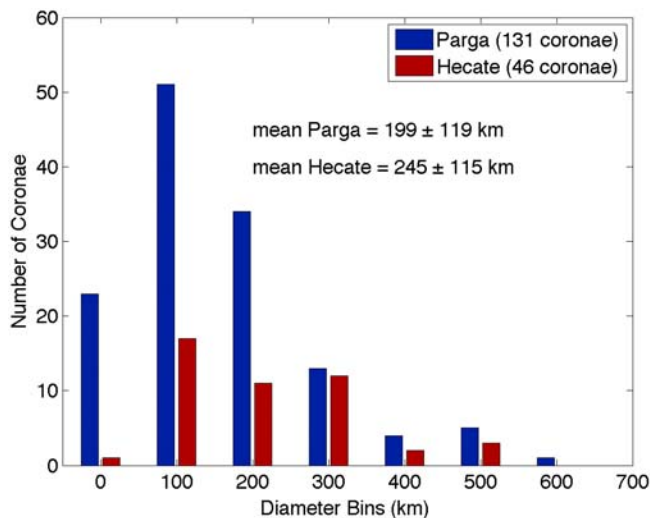
Figure 8. Histogram of diameters of coronae in Hecate and Parga chasmata.

[46] *Hoogenboom et al.* [2005] examined elastic thickness estimates versus corona age relative to rifting using 31 coronae, primarily from Parga and Hecate chasmata. Their study was confined to larger coronae as they examined the gravity signatures from individual coronae. They found a general trend for coronae older than the rift to have low values of T_e (0–19 km) and coronae that formed before the rifts to have larger T_e values (0–56 km). The elastic thickness values they found for individual coronae are in good agreement with values found in this study. However, when looking at the coronae over the full range of sizes at Parga and Hecate chasmata seen in this study, this trend is not maintained (see Figure 7).

3.3. Comparison Between Coronae in Parga and Hecate and the Global Population

[47] The populations of coronae at Parga and Hecate have similarities and differences. The most striking is that there are 131 coronae along or near Parga chasma but Hecate chasma has only 50 coronae. Note that two coronae (located at 8°S, 24.3°E and 2.5°N, 22.2°E) are double counted as it is unclear whether they are better assigned to Hecate or Parga chasmata. Although Hecate chasma is about 20% shorter than Parga chasma (8000 km versus 10,000 km, respectively), Parga still has proportionately many more coronae (see Figures 7 and 8). Additionally, the population of coronae is, on average, smaller in diameter at Parga than at Hecate. Proportionally, Parga has many more coronae of less than 100 km in diameter and fewer with diameters greater than 300 km than Hecate (Figure 8). The average diameter and standard deviation of coronae in Parga is 199 ± 119 km versus 245 ± 115 km at Hecate.

[48] Examining the coronae at Parga chasma as a function of diameter suggests differences in the population of coronae of less than approximately 300 km in size compared with the larger coronae. Figure 9 shows a large majority of smaller coronae that have low amounts of volcanism, are relatively young with respect to the associated rift, and have a concentric shape. Note that there are 55 coronae in the Parga chasma region that are not located along the rift and thus do

not have a stratigraphic age relative to the rift. At Hecate chasma, coronae of less than 200 km are more likely to have low amounts of volcanism (Figure 10). The age of coronae relative to the rift is not a strong function of diameter, though more coronae of less than 300 km in diameter are classified as forming synchronously with the rift than before or after rift formation. Both Hecate (Figure 10) and Parga chasmata (Figure 9) have similar feature type versus diameter distributions. This distribution is typical of the corona population as a whole [*Stofan et al.*, 1992, 2001].

[49] The majority (62%) of the global population of coronae is found in fracture zones, either major rifts or more minor fracture zones [*Glaze et al.*, 2003]. Other coronae are distributed between hot spot regions (11%) and plains (25%). *Glaze et al.* [2003] found that the diameters of coronae at fracture zones and in the plains are on average closer to 210 km, while those at hot spots are closer to 250 km on average. Given that approximately 40% of coronae in fracture zones (25% of the entire corona population) occur in Parga chasma, it is not surprising that the average diameter observed at Parga chasma is similar to that of the overall population of coronae at fracture zones. However, it is surprising that the Hecate population is closer in average diameter to the global population of coronae than those in fracture settings. Another interesting aspect of the corona populations is that there are numerous examples of chains or clusters of coronae of similar size (Figure 7). We discuss possible implications of these different populations below.

[50] The size, relative age, and high concentration of coronae at Parga Chastmata suggest that coronae have been forming over an extended time, possibly via different mechanisms. The majority of coronae at Parga are less than 200 km in diameter. Many of the rift segments (P4, P6, and P11, see Figure 7b) have associated coronae that are similar in size distributed along their length. Other small coronae off the rift (e.g., 0°N, 233–253°E) are generally aligned and similar in size. This pattern suggests that instabilities may be contributing to the formation of coronae in this region. Many researchers have studied the formation of melt in extensional environments, including melting in periodically spaced upwellings. *Hernlund et al.* [2008a, 2008b] modeled the development of melting during both active extension and in a second phase that occurs once extension has stopped. The timing and amount of melting predicted is a function of extension rate, melt percolation, and the depth distribution of solid density variations arising from melt depletion. The development of a second melt phase following extension is favored by a faster rate of extension, higher mantle viscosity, higher rate of melt percolation, and smaller amounts of solid residuum depletion-derived buoyancy. Spacing between melting instability upwellings is ~2–3 times the thickness of the partially molten layer.

[51] The low amount of associated volcanism and relatively young stratigraphic age (with respect to the rift) of many of the small coronae at Parga are consistent with their formation via melt instabilities as opposed to a primary thermal upwelling. The large number of small coronae and the highly variable lithospheric structure suggest that they may be due to a second stage of extension-related melting. This interpretation is based in part on the comparison to Hecate chasma, where the lithospheric structure still clearly reflects the extensional environment and there are many fewer coronae.
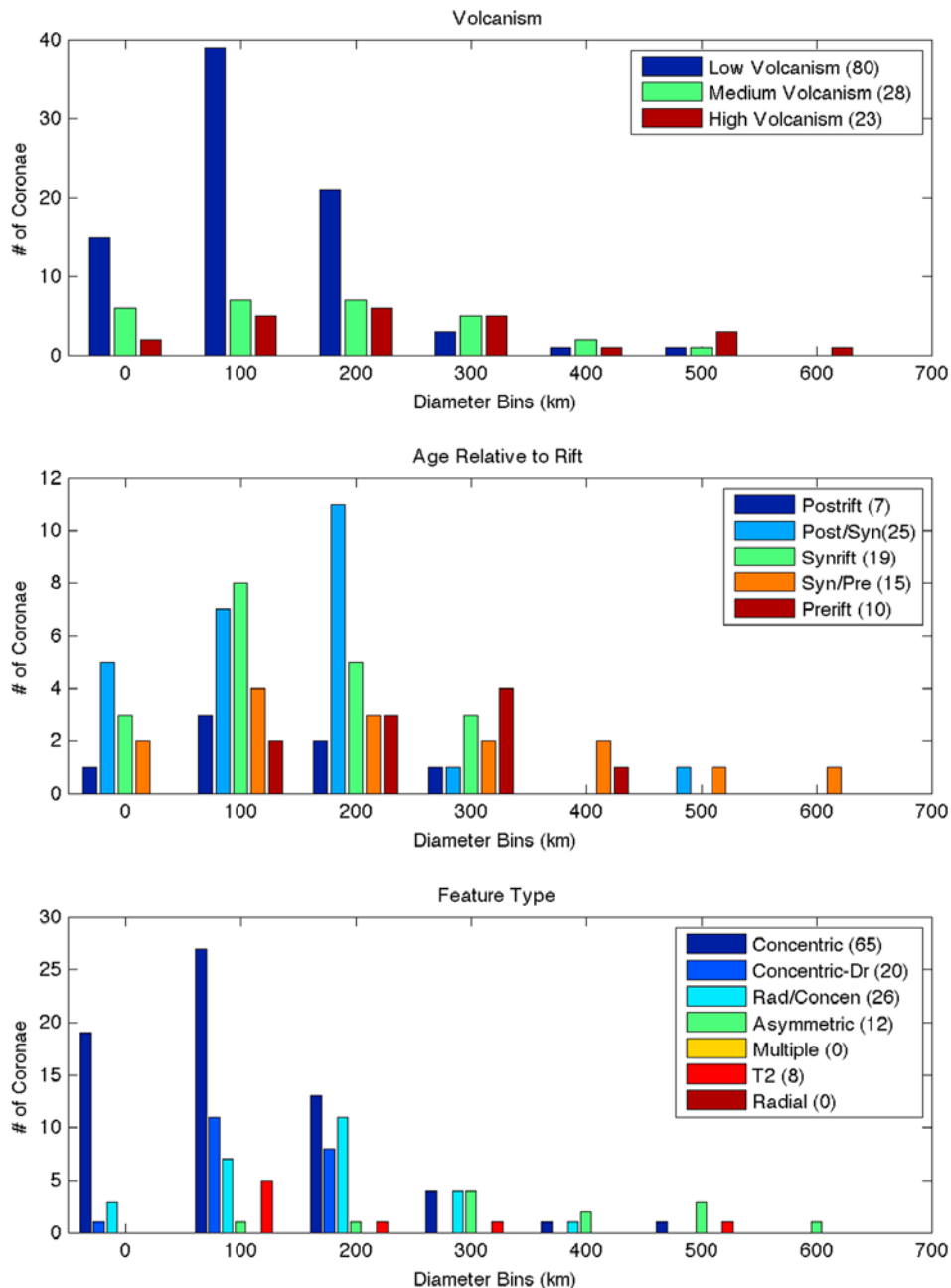
Figure 9. Histograms of the amount of volcanism, the stratigraphic age of the corona relative to the rift, and the fracture shape of coronae as a function of diameter in Parga chasma. Note that only 61 coronae intersect the rift, and thus only those coronae have a relative age.

Additionally, *Elkins-Tanton and Furman* [2008] have discussed the potential for periodic lithospheric delamination instabilities to form adjacent to rifts. Such a mechanism would also develop some time after the lithosphere has begun to extend. These two mechanisms for diapiric upwelling and downwellings could account for the chains of coronae observed at Parga.

[52] The area of Parga chasma between Atete and Maram coronae is anomalous in several regards. The ADC in this area (see Figure 7d) is locally quite low, with a best fit value of 21 km, yet the best fit elastic thickness is 45 km (admittance class 9). This unusual combination of values along with the admittance curves suggests that dynamic processes are affecting the gravity signature. The admittance curves for Parga (Figure 2) show that classes 7 and 9 and, to a lesser degree, class 6 have a steep admittance curve. Additionally, *Mueller et al.* [2008] observe both high and low emissivity anomalies in this region. Low emissivity anomalies are commonly found in association with tessera terrain, and high emissivity anomalies are in association with volcanoes and coronae. *Mueller et al.* [2008] interpret low emissivity anomalies as possibly due to compositional variations and high emissivity anomalies as likely due to a lack of weathering due to relatively recent activity. The location of both low and high
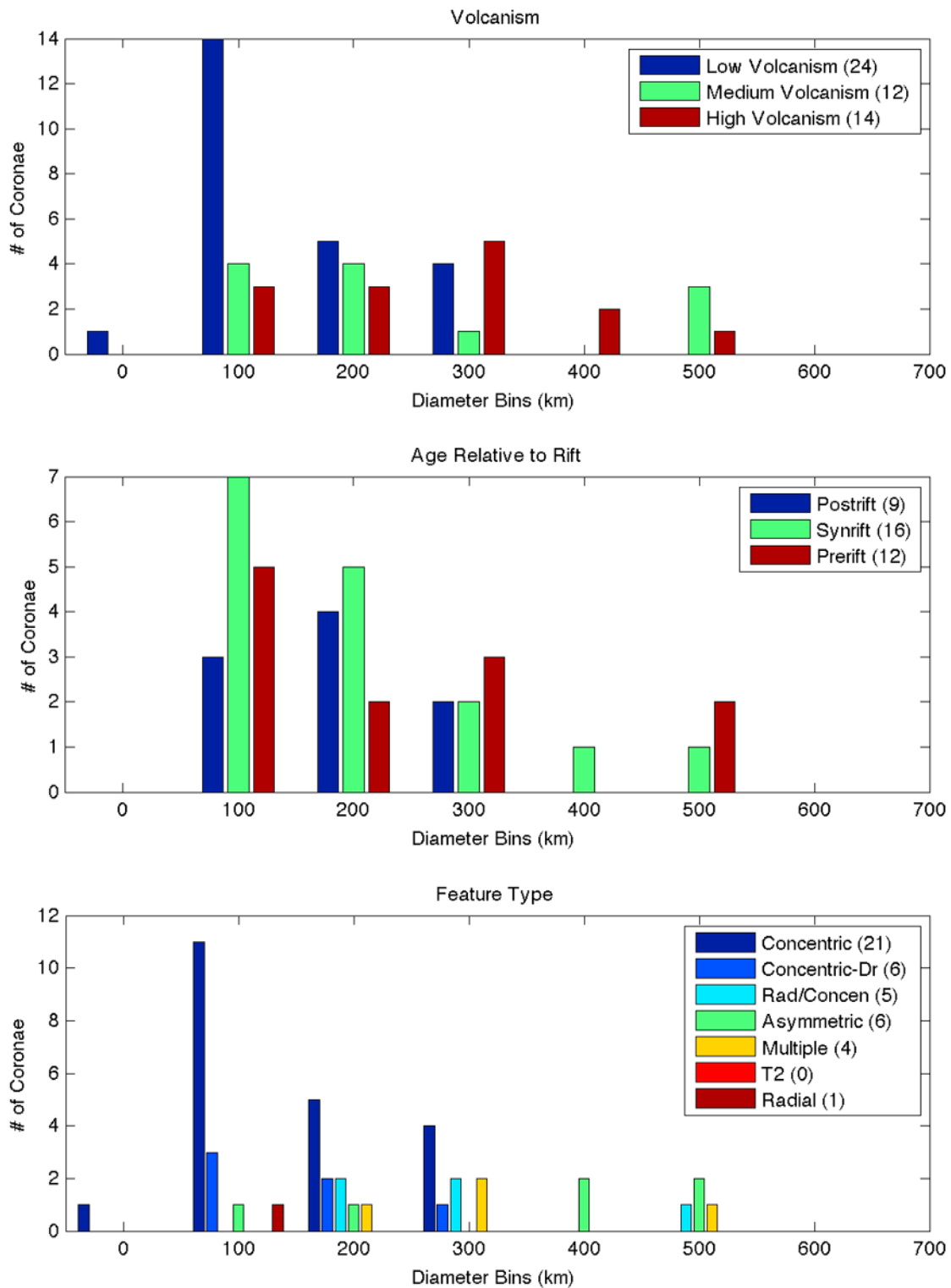
Figure 10. Histograms of the relative stratigraphic age of coronae relative to the rift (34 coronae intersect the rift) and feature type as a function of diameter for coronae in the Hecate chasma area.

anomalies at Atete is unusual and may suggest both unusual (perhaps more felsic) composition and relatively recent flows, respectively. More felsic melt compositions are predicted to occur at sites of delamination on Venus [*Elkins-Tanton et al.*, 2007].

[53] Although there is no constraint on absolute ages, we interpret Hecate as likely to be currently extending [*Smrekar et al.*, 2009] and Parga as likely to be either inactive or in a later stage of evolution. The thin elastic lithosphere and shallow ADC (see Figures 7b and 7d) correlated with the

topographic rise at Themis Regio suggest that it is active and underlain with upwellings on the scale of the coronae. At Hecate, there is a broad region associated with one of the branches that has a very low elastic thickness. This is consistent with high heat flow in this region, although it is not a unique interpretation. This region may also be isostatically compensated, such that there is no flexural signature and the derived value of elastic thickness is meaningless. In either case, the relatively low ADC in this region indicates that there is no active upwelling at the scale of the rift. As discussed above, the relatively large elastic thickness and better-developed fracture system along the main branch of Hecate suggest more crustal thinning, which would bring the mantle to shallower depths and increase the effective elastic thickness [*Burov and Diament*, 1995].

[54] We interpret the complexity of Parga chasma's branches and lithospheric structure and the large number of coronae to indicate a late stage of development. Many of the smaller coronae may have formed as the extensional system developed, allowing secondary melting and possibly delamination to occur. The lithospheric structure associated with rifting at Hecate may have never developed at Parga or been disrupted by subsequent modification by pressure release melting and delamination.

4. Conclusions

[55] We examine the lithospheric structure and corona population at the two largest rift systems on Venus, Parga, and Hecate chasmata. The derived estimates of both ADC and elastic thickness have very different spatial distributions at Parga and Hecate chasmata, as well as somewhat different ranges. Neither rift system has a large ADC, implying that there is no regional scale upwelling associated with the system.

[56] At Hecate chasma, lithospheric structure is generally correlated with two of the main segments of the rift. The northwestern region has very low elastic thickness (~0 km) and moderate ADC (~50 km). The main rift has moderate elastic thickness (~40–60 km) and low ADC (~30–50 km). The coronae and fractures in these two regions are also distinct [*Hamilton and Stofan*, 1996]. The northwest region has more diffuse fractures and extensive volcanism, and coronae tend to be plateau shaped and display radial graben. In the central region, the fractures are typically well-defined graben and single normal faults, and many coronae have central depressions or raised rims and fracture annuli. We interpret these results and correlations to indicate that there is likely active extension at Hecate chasma. One interpretation of the thin crust and thick elastic lithosphere is that extension has progressed sufficiently along the main branch to thin the crust and bring the mantle closer to the surface, similar to other analysis of rift zones on Venus [e.g., *Rathbun et al.*, 1999; *Kiefer and Swafford*, 2006]. Although difficult to estimate, the surface expression of extension does not suggest large amounts of strain. Extension history in Hecate will be explored in a follow-on paper. The larger amount of volcanism and greater number of coronae with positive relief in the northwestern region is consistent with the interpretation that the low elastic thickness may indicate higher heat flow rather than isostasy. Impact crater densities also suggest that Hecate is a relatively young area [*Phillips and Izenberg*, 1995].

[57] In most regions, lithospheric structure along Parga chasma is indistinct from that of the surrounding areas. One exception occurs in a section of the chasma between Atete and Maram coronae, the two largest coronae in Parga chasma. This section has regions of very low ADC, though it is not uniform across the segment. The unusual values of elastic thickness and ADC, as well as the steep admittance curves in this region, suggest that dynamic processes are likely to be affecting the gravity signature. Themis Regio also shows distinct lithospheric properties, with a low elastic thickness and intermediate ADC. The intermediate ADC appears characteristic of large volcanic rises dominated by coronae, suggesting numerous small-scale plumes associated with the coronae rather than a single plume on the scale of the topographic rise. The low elastic thickness at Themis is also likely to imply high heat flow.

[58] The differences in the corona populations at Parga and Hecate chasmata also offer some insight into the relationship between rifting and corona formation. These two populations represent 35% of all coronae and 56% of coronae associated with fracture zones. The number of coronae at Parga chasma (131) is very large as compared to the number in Hecate (50). The population of coronae at Parga is on average smaller (average diameter = 199 ± 119 km) than that at Hecate (average diameter = 236 ± 120 km). Smaller coronae are typically younger with respect to the rift and have less volcanism. This trend is especially pronounced at Parga chasma. Although there are only 23 coronae larger than 300 km in diameter at Parga, they are equally likely to have low, medium, or high volcanism and are slightly more likely to be stratigraphically older relative to the rift. The numbers are smaller at Hecate, but the same observations hold. Another feature of the many small coronae at both chasmata is that there are a number of chains of similar diameter, typically along a given branch of the rift. We interpret observations to indicate that the smaller coronae may form via a different process than the larger coronae.

[59] The fact that smaller coronae tend to be relatively young compared with the rift suggests that they may be the result of post rift extension-driven pressure release melting [*Hernlund et al.*, 2008a, 2008b]. The larger coronae may form above larger upwellings from a thermal boundary layer. If many of the coronae are formed via diapiric upwelling in a broad region of extension, this could explain why *Martin et al.* [2007] did not find a correlation between the location of the rift fractures and the coronae, since melting might occur over a broader zone than the fracturing. A greater amount of diapiric melting at Parga relative to Hecate could be due to the prerifting lithospheric structure or the rate of extension or might indicate that Parga is in a later stage of evolution. If the latter, such melting may occur at Hecate in the future if extension rate, lithospheric structure and composition are favorable. We note that the low number of impact craters [*Phillips et al.*, 1992] and especially dark halo craters [*Phillips and Izenberg*, 1995] are consistent with Hecate being a relatively young area. The good correspondence between the gravity signature and major rift segments at Hecate also suggests that extension is an active process, as explored by *Smrekar et al.* [2009].

[60] The analysis of these two rift systems shows that relationship between lithospheric structure, rifting, and corona formation varies from region to region and may point to

differing formation mechanisms for coronae in rift zones, including primary diapirs from depth, diapirs due to decompression melting, and diapirs due to lithospheric delamination along the margins of rift systems. Neither rift has a large compensation depth, implying that there is no broad-scale active upwelling. The forces driving regional extension on such large scales remain elusive.

References

Anderson, F. S. and W. B. Banerdt (2000), Preliminary admittance estimates for the Valles Marineris, Mars, in *Lunar and Planetary Science XXXI*, Lunar and Planetary Institute, Houston (CD-ROM), Abstract 2090.

Anderson, F. S. and S. E. Smrekar (2006), Global mapping of crustal and lithospheric thickness on Venus, *J. Geophys. Res. Planets*, 111(E8), E08006, doi:10.1029/2004JE002395.

Baer, G., G. Schubert, D. L. Bindschadler and E. R. Stofan (1994), Spatial and temporal relations between coronae and extensional belts, Northern Lada-Terra, Venus, *J. Geophys. Res.*, 99(E4), 8835–8369.

Banks, R. J., and C. J. Swain (1978), The isostatic compensation of East Africa, *Proc. R. Soc. London, A*, 364, 331–352.

Barnett, D. N., F. Nimmo, and D. McKenzie (2000), Flexure of Venusian lithosphere measured from residual topography and gravity, *Icarus*, 16, 404–419.

Basilevsky, A. T., A. A. Pronin, L. B. Ronca, V. Kryuchkov, A. L. Sukhanov and M. S. Markov (1986), Styles of tectonic deformation on Venus: Analysis of Veneras 15 and 16 data, *J. Geophys. Res.*, 91(B4), 399–411.

Bleamaster, L. F. and V. L. Hansen (2004), Effects of crustal heterogeneity on the surface morphology of chasmata, Venus. *J. Geophys. Res.*, 109(E2), EO2004, doi:10.1029/2003JE002193.

Brian, A. W., E. R. Stofan, J. E. Guest, and S. E. Smrekar (2004), Laufey Regio: A newly discovered topographic rise on Venus, *J. Geophys. Res.*, 109(E7), E07002, doi:10.1029/2002JE002010.

Burov, E. B. and M. Diament (1995), The effective elastic thickness of continental lithosphere: What does it really mean?, *J. Geophys. Res.*, 100(B3), 3905–3927.

Crumpler, L. S., J. W. Head and J. C. Aubele (1993), Relation of major volcanic centre concentration on Venus to global tectonic patterns, *Science*, 261, 591–594.

Crumpler, L. S., et al. (1997), Volcanoes and centers of volcanism on Venus, in *Venus II*, edited by S. W. Brougher et al., pp. 697–756, Univ. of Ariz. Press, Tucson, Ariz.

Cyr, K. E. and H. J. Melosh (1993), Tectonic patterns and regional stresses near Venusian coronae, *Icarus*, 102, 175–184.

Dombard, A. J., C. L. Johnson, M. A. Richards and S. C. Solomon (2007), A magmatic loading model for coronae on Venus, *J. Geophys. Res.*, 112(E4), E04006, doi:10.1029/2006JE002731.

Dorman, L. M., and B. T. R. Lewis (1970), Experimental isostasy: I. Theory of the determination of the Earth's isostatic response to a concentrated load, *J. Geophys. Res.*, 75(17), 3357–3365.

Elkins-Tanton, L., and T. Furman (2008), Lithospheric processes that enhance melting at rifts, AGU, Fall Meeting 2008, abstract T31D-07.

Elkins-Tanton, L., S. E. Smrekar, P. C. Hess and E. M. Parmentier (2007), Volcanism and volatile recycling on a one-plate planet: Applications to Venus, *J. Geophys. Res.*, 112(E4), E04S06, doi:10.1029/2006JE002793.

Forsyth, D. W. (1985), Sub-surface loading and estimates of the flexural rigidity of the continental lithosphere, *J. Geophysics. Res.*, 90(B14), 12623–12632.

Glaze, L. S., E. R. Stofan, S. E. Smrekar and S. M. Bologa (2003), Insights into corona formation through statistical analyses, *J. Geophys. Res.*, 107(E12), 5135, doi:10.1029/2002JE001904.

Grimm, R. E., and P. C. Hess (1997), The crust of Venus, in *Venus II*, edited by S. W. Bougher, D. M. Hunten, and R. J. Phillips, pp. 1205–1244, Univ. of Ariz. Press, Tucson, Ariz.

Grindrod, P. M., E. R. Stofan, A. W. Brian, and J. E. Guest (2006), The geological evolution of Atia Mons,Venus: a volcano-corona "hybrid", *J. Geol. Soc.*, 163, 265–275.

Hamilton, V., and E. R. Stofan (1996), The geomorphology and evolution of Hecate chasma, Venus, *Icarus*, 121, 171–194.

Hansen, V. L. (2000), Geologic mapping of tectonic planets, *Earth Planet. Sci. Lett.*, 176, 527–542.

Hansen, V. L. (2003), Venus diapers: Thermal or compositional?, *Geol. Soc. Am. Bull.*, 115, 1040–1052.

Hansen, V. L., and R. J. Phillips (1993), Tectonics and volcanism of Eastern Aphrodite Terra, Venus: No subduction, no spreading, *Science*, 260, 526–530.

Head, J. W., L. S. Crumpler, J. C. Aubele, J. E. Guest, and R. S Saunders (1992), Venus volcanism: Classification of volcanic features and structures, associations, and global distributions from Magellan data, *J. Geophys. Res.*, 97(E8), 13,153–13,197.

Hernlund, J. W., P. J. Tackley, and D. J. Stevenson (2008a), Bouyant melting instabilities beneath extending lithosphere: 1. Numerical models, *J. Geophys. Res.*, 113(B4), B04405, doi:10.1029/2006JB004862.

Hernlund, J. W., D. J. Stevenson, and P. J. Tackley (2008b), Bouyant melting instabilities beneath extending lithosphere: 2. Linear analysis, *J. Geophys. Res.*, 113(B4), B04405, doi:10.1029/2006JB004863.

Herrick, R. R. (1999), Small mantle upwellings are pervasive on Venus and Earth, *Geophys. Res. Lett.*, 26(6), 803–806.

Herrick, R. R., and R. J. Phillips (1992), Geologic correlations with the interior density structure of Venus, *J. Geophys. Res.*, 97(E10), 16,017–16,034.

Herrick, R. R., J. Dufek, and P. J. McGovern (2005), Evolution of large shield volcanoes on Venus, *J. Geophys. Res.*, 110(E1), E01002, doi:10.1029/2004JE002283.

Hieronymus, C. F., and D. Bercovici (2000), Non-hotspot formation of volcanic chains: control of tectonic and flexural stresses on magma transport, *Earth Planet. Sci. Lett.*, 181, 539–554.

Hoogenboom, T. and G. A. Houseman (2006), Rayleigh-Taylor instability as a mechanism for corona formation on Venus, *Icarus*, 180(2), pp. 292–307, doi:10.1016/j.icarus.2005.11.001.

Hoogenboom, T., G. Houseman, and P. Martin (2005), Elastic thickness estimates for coronae associated with chasmata on Venus, *J. Geophys. Res.*, 110(E9), E09003, doi:10.1029/2004JE002394.

Janes, D. M., S. W. Squyres, D. L. Bindschadler, G. Baer, G. Schubert, V. L. Sharpton, and E. R. Stofan (1992), Geophysical models for the formation and evolution of coronae on Venus, *J. Geophys. Res.*, 97(E10), 16,055–16,067.

Johnson, C. L., and D. T. Sandwell (1994), Lithospheric flexure on Venus, *Geophys. J. Int.*, 119, 627–647.

Kiefer, W. S., and B. H. Hager (1992), Geoid anomalies and dynamic topography from convection in cylindrical geometry: applications to mantle plumes on Earth and Venus, *Geophys. J. Int.*, 108, 198–214.

Kiefer, W. S., and L. C. Swafford (2006), Topographic analysis of Devana chasma, Venus: implications for rift system segmentation and propagation, *J. Struct. Geol.*, 28, 2144–2155.

Koch, D. M., and M. Manga (1996), Neutrally buoyant diapirs: A model for Venus coronae, *Geophys. Res. Lett.*, 23(3), 220–228.

Konopliv, A. S., W. S. Banerdt, and W. L. Sjogren (1999), Venus gravity: 180th degree and order model, *Icarus*, 139, 3–18.

Lowry, A. R. and R. B. Smith (1994), Flexural rigidity of the Basin and Range-Colorado Plateau-Rocky Mountain transition from coherence analysis of gravity and topography, *J. Geophys. Res.*, 99(B10), 20,123–20,140.

Martin, P. E. R. Stofan, L. S. Glaze, and S. E. Smrekar (2007), Coronae of Parga chasma, Venus. *J. Geophys. Res.*, 112(E4), EO4S03, doi:10.1029/2006JE002758.

McGill, G. E. (1994), Hotspot evolution and Venusian tectonic style, *J. Geophys. Res.*, 99(E11), 23,149–23,161.

McKenzie, D. and D. Fairhead (1997), Estimates of the effective elastic thickness of the continental lithosphere from Bouguer and free air gravity anomalies, *J. Geophys. Res.*, 102(B12), 27,523–27,552.

McKenzie, D., and F. Nimmo (1997), Elastic thickness estimates for Venus from line of sight accelerations, *Icarus*, 130, 198–216.

McKenzie, D. P., and C. Bowin (1976), The relationship between bathymetry and gravity in the Atlantic Ocean, *J. Geophys. Res.*, 81(11), 1903–1915.

McNutt, M. K. (1983), Influence of plate subduction on isostatic compensation in northern California, *Tectonics*, 2(4), 399–415.

McNutt, M. K. (1988), Thermal and mechanical properties of the Cape Verde rise, *J. Geophys. Res.*, 93(B4), 2784–2794.

Moresi, L., and B. Parsons (1995), Interpreting gravity, geoid, and topography for convection with temperature-dependent viscosity - Application to surface features on Venus, *J. Geophys. Res.*, 100(E10), 21155–21171.

Mueller, N., J. Helbert, G. L. Hashimoto, C. C. C. Tsang, S. Erard, G. Piccioni, P. Drossart (2008), Venus surface thermal emission at 1 μ m in VIRTIS imaging observations: Evidence for variation of crust and mantle differentiation conditions, *J. Geophys. Res.*, 114(E5), E00B17, doi:10.1029/2008JE003118.

Nimmo, F., and D. McKenzie (1996), Modeling plume-related uplift, gravity and melting on Venus, *Earth Planet. Sci. Lett.*, *145*, 109–123.

Petit, C., and C. Ebinger (2000), Flexure and mechanical behavior of carbonic lithosphere: gravity models of the East African and Baikal Rifts, *J. Geophys. Res.*, *105*(B8), 19151–19162.

Phillips, R. J., and N. R. Izenberg (1995), Ejecta correlations with spatial crater density and Venus resurfacing history, *Geophys. Res. Lett.*, *22*(12), 1517–1520.

Phillips, R. J., R. F. Raubertas, R. E. Arvidson, I. C. Sarker, R. R. Herrick, N. R. Izenberg, and R. E. Grimm (1992), Impact craters and Venus resurfacing history, *J. Geophys. Res.*, *97*(E10), 15,923–15,948.

Rappaport, N., and J. J. Plaut (1994), A 360-order model of Venus topography, *Icarus*, *112*, 27–33.

Rathbun, J. A., D. M. Janes, and S. W. Squyres (1999), Formation of Beta Regio, Venus: results from measuring strain, *J. Geophys. Res.*, *104*(E1), 1917–1927.

Robinson, E. M., and B. Parsons (1988), Effect of a shallow low-viscosity zone on the formation of mid-plate swells, *J. Geophys. Res.*, *93*(B4), 3144–3156.

Sandwell, D. T., and G. Schubert (1992a), Flexural ridges, trenches, and outer rises around Venus coronae, *J. Geophys. Res.*, *97*(E10), 16069–16083.

Sandwell, D. T., and G. Schubert (1992b), Evidence for retrograde subduction on Venus, *Science*, *257*, 766–770.

Sheehan, A. F., and M. K. McNutt (1989), Constraints on thermal and mechanical structure of the oceanic lithosphere at the Bermuda Rise from geoid height and depth anomalies, *Earth Planet. Sci. Lett.*, *93*, 377–391.

Simons, M., B. H. Hager, and S. C. Solomon (1994), Global variations in geoid/topography admittances on Venus, *Science*, *256*, 798–803.

Simons, M., S. C. Solomon and B. H. Hager (1997), Localization of the gravity and topography constraints on the tectonics and mantle dynamics of Venus, *Geophys. J. Int.*, *131*, 24–44.

Simons, F. J., M. T. Zuber, and J. C. Korenaga (2000), Isostatic response of the Australian lithosphere: Estimation of effective elastic thickness and anisotropy using multi-taper spectral analysis, *J. Geophys. Res.*, *105*(B8), 19,163–19,184.

Smrekar, S. E. (1994), Evidence for active hotspots on Venus from analysis of Magellan gravity data, *Icarus*, *112*, 2–26.

Smrekar, S. E., and R. J. Phillips (1991), Venusian highlands: Geoid to topography ratios and their implications, *Earth Planet. Sci. Lett.*, *107*, 582–597.

Smrekar, S. E. and E. R. Stofan (1997), Corona formation and heat loss on Venus by coupled upwelling and delamination, *Science*, *277*, 1289–1294.

Smrekar, S. E., and E. R. Stofan (1999), Origin of corona-dominated topographic rises on Venus, *Icarus*, *139*, 100–116.

Smrekar, S. E., and E. R. Stofan (2003), Effects of lithospheric properties on the formation of type 2 coronae on Venus, *J. Geophys. Res.*, *108*(E8), 5091, doi:10.1029/2002JE001930.

Smrekar, S. E., E. R. Stofan, and W. S. Kiefer (1997), Large volcanic rises on Venus, in *Venus II*, edited by S. W. Bougher, D. M. Hunten, and R. J. Phillips, pp. 845–878, Univ. of Arizona Press, Tucson, Ariz.

Smrekar, S. E., R. Comstock, and F. S. Anderson (2003), A gravity survey of type 2 coronae on Venus, *J. Geophys. Res.*, *108*(E8), 5090, doi:10.1029/2002JE001935.

Smrekar, S. E., E. Stofan, P. Martin, T. Hoogenboom, and R. Buck (2009), Models of Hecate chasma Venus and implications for active extension, *41st Lunar and Planetary Science Conf. (2010), Abstract #1422, 2pp*, Lunar and Planetary Institute, Houston (CD-ROM).

Stofan, E. R., and S. E. Smrekar (2005), Large topographic rises, coronae, large flow fields and large volcanoes on Venus: Evidence for mantle plumes?, in *Plates, Plumes, and Paradigms*, edited by G. R. Foulger et al., *Geol. Soc. Am.*, vol. 388, pp. 861.

Stofan, E. R., D. L. Bindschadler, J. W. Head, and E. M. Parmentier (1991), Corona structures on Venus: Models of origin, *J. Geophys. Res.*, *96*(E4), 20,933–20,946.

Stofan, E. R., V. L. Sharpton, G. Schubert, G. D. Baer, D. L. Bindschadler, D. M. Janes and S. W. Squyres (1992), Global distribution and characteristics of coronae and related features on Venus: Implications for origin and relation to mantle processes, *J. Geophys. Res.*, *97*(E8), 13,347–13,378.

Stofan, E. R., V. E. Hamilton, D. M. Janes, and S. E. Smrekar (1997), Coronae on Venus: Morphology and Origin, in *Venus II*, edited by S. W. Brougher, D. M. Hunten, and R. J. Phillips, pp. 931–965, Univ. of Ariz. Press, Tucson, Ariz.

Stofan, E. R., S. E. Smrekar, S. W. Tapper, J. E. Guest, and P. Grindrod (2001), Preliminary analysis of an expanded corona database for Venus, *Geophys. Res. Lett.*, *28*(22), 4267–4270, doi:10.1029/2001GL013608.

Tackley, P. J., and D. J. Stevenson (1991), The production of small Venusian coronae by Rayleigh Taylor instabilities in the uppermost mantle, *EOS Trans. AGU*, *72*, 287.

Tackley, P. J. and D. J. Stevenson (1993), A mechanism for spontaneous self-perpetuating volcanism on the terrestrial planets, in *Flow and Creep in the Solar System: Observations, Modeling and Theory*, edited by D. B. Stone and S. K. Runcorn, pp. 307–322, Kluwer Acad., Norwell, Mass.

Tou, J. T., and R. C. Gonzalez (1974), *Pattern Recognition Principles*, 377 pp., Addison Wesley-Longman, Reading, Mass.

Watts, A. B., J. H. Bodine and M. S. Steckler (1980), Observations of flexure and the state of stress in the oceanic lithosphere, *J. Geophys. Res.*, *85*(B11), 6369–6376.

Zuber, M. T., T. D. Bechtel and W. D. Forsyth (1989), Effective elastic thickness of the lithosphere and mechanisms of isostatic compensation in Australia, *J. Geophys. Res.*, *94*(B7), 9353–9367.

T. Hoogenboom, ExxonMobil, Gravity-Magnetics Group, 233 Benmar Street, Houston, TX 77060, USA.

P. Martin, Department of Earth Sciences, Durham University, Science Laboratories, South Road, Durham DH1 3LE, UK.

S. E. Smrekar, Jet Propulsion Laboratory, California Institute of Technology, Mail Stop 183-501, 4800 Oak Grove Drive, Pasadena, CA 91109, USA. (ssmrekar@jpl.nasa.gov)

E. R. Stofan, Proxemy Research, 20528 Farcroft Lane, Laytonsville, MD 20882, USA.